

Chapter 4

Ceric Oxide (CeO₂)

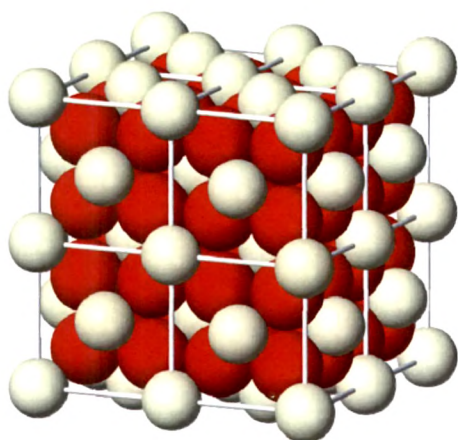
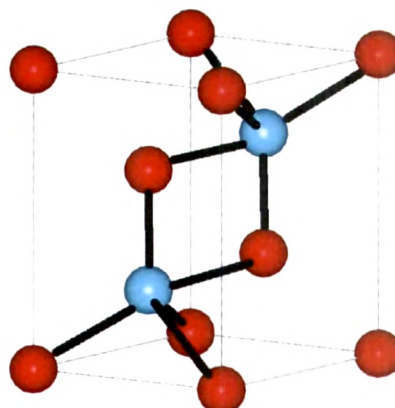
4.1 Introduction

Systems involving rare earth oxides, especially Cerium, have many practical applications due to their excellent physical and chemical properties. The most stable oxide of Cerium is Cerium dioxide, CeO₂. When Cerium salts are calcined in air or oxygen-containing environments, the tetravalent Ce(IV) oxide is formed ^[1]. In recent years, Cerium oxide (CeO₂) powders have attracted much attention owing to their potential uses in a variety of applications, e.g. UV absorbents and filters ^[2, 3], as catalysts for the treatment of automotive exhaust system because of its high oxygen ion conductivity ^[4] and petroleum-cracking catalyst ^[5]. Rare-earth-doped Ceria have been considered promising materials as oxygen ion conducting electrolytes or electrodes for Solid Oxide Fuel Cell (SOFC) ^[6], oxygen pumps ^[7, 8] and oxygen sensors ^[9]. It is also used as polishing agents for the chemical mechanical planarization (CMP) process, gate oxides in metal oxide semiconductor devices and ultraviolet (UV) blocking materials in UV shielding ^[10, 11]. Ceria nano particles are being used in many biomedical applications due to their nontoxic nature and excellent biocompatibility ^[12]. However, Ceria shows weak emission characteristics that limits its identification in biological and cellular studies. To improve its luminescence properties for biological application, a tag such as fluorescent dye is attached like a shell to the surface of the nanoparticle. In the process, modification of the surface takes place and this leads to biological inactivity of the nanoparticle. It also makes the material more bulky and thus limits the penetration of the cells by the nanoparticles. Secondary approach involves doping of the parent matrix with elements that can emit itself upon excitation in UV-visible range of spectrum ^[13].

The oxides of Cerium are available in two different forms, Ceric oxide (CeO₂) and Cerrous oxide (Ce₂O₃) ^[14]. In the former, the valence state of Cerium is +4 and in the later it is +3. Ceric oxide is formed by calcining Cerium oxalate or Cerium hydroxide. Powdered Ceria is slightly hygroscopic and will also absorb small amount of carbon dioxide from the

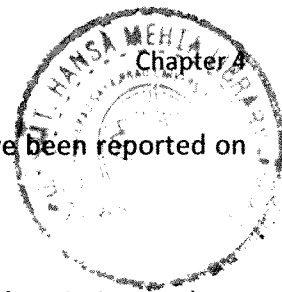
atmosphere. Amongst the two forms available, the most stable phase is CeO_2 at room temperature and under standard atmospheric conditions. CeO_2 crystallizes having the fluorite CaF_2 cubic type structure. This structure is RX_2 type, where R is especially big and located at the center of the eight X atoms situated at the corners of a surrounding cube and each X atom has about it a tetrahedron of R atoms. For spherical atoms, contact between an R atom and its eight coordinated X atoms would occur only when the radius of R is greater than 0.73 times that of X i.e. $r(\text{R}) / r(\text{X}) \geq 0.73$. This relation is valid in the compounds with the fluorite arrangement ^[15]. In CeO_2 , Ce^{4+} cation is located at the centre and is surrounded by eight equivalent O^{2-} ions forming the corner of the cube with each O^{2-} ion coordinated to four Ce^{4+} ions. It can be regarded as consisting of CeO_8 cubes sharing each edge with an adjacent cube. Alternatively, the structure can be described as OCe_4 tetrahedra sharing their edges with adjacent OCe_4 tetrahedra. The space group for CeO_2 is $Fm\bar{3}m$ and its lattice constant is 0.54110 nm. As there is only one kind of Ce-O bond in CeO_2 , only one broad charge transfer excitation peak is observed. The coordination number of Ce^{4+} to O^{2-} reduces from eight to seven and introduces Ce^{3+} ions into the crystal lattice. Ce^{3+} ions have a higher ionic radius (1.034 Å) as compared to the Ce^{4+} ions (0.92 Å). The introduction of the oxygen vacancies and the accompanying Ce^{3+} ions leads to a distortion of the local symmetry. This causes change in the Ce – O bond length (lattice distortion) and the overall lattice parameter. Some properties, structure and structural parameters of both the forms of oxides are given below.

Formula	Molar mass	Appearance	Density	Melting point	Crystal structure	Space group
CeO_2	172.11 g/mol	White or pale yellow	7.215 g/cm ³	2400°C	Cubic (fluorite)	$Fm\bar{3}m$
Ce_2O_3	328.24 g/mol	Yellow	6.2 g/cm ³	2177°C	Hexagonal	P-3m1

Structure of CeO_2 Structure of Ce_2O_3

Europium belongs to the rare earth metal group and has a strong red emission when doped in different matrices. Europium is considered as a suitable dopant for enhancing emission in Ceria for three reasons: (i) it can be excited in a wide range of wavelengths from ultraviolet to visible light,^[16] (ii) the ionic radius [13clum] of Eu^{3+} (0.1066 nm), being close to that of Cerium (Ce^{3+} , 0.1143 nm; Ce^{4+} , 0.097 nm), favors extensive solubility with the Ceria lattice, and (iii) it increases the trivalent state of Cerium, which may further enhance the applicability of Ceria. Therefore Europium doped Ceria can be used in fluorescence applications. Terbium in the +3 valence state has an ionic radius of 0.1063 nm. Hence the solubility in the Ceria lattice is appreciable. It also shows absorption in the UV and visible region and emission at its characteristic green wavelength but the yield is not appreciable.

Cerium provides strong absorption below 400 nm caused by charge transfer bands^[17]. Due to its high refractive index, optical transparency, thermal and chemical stability, high dielectric constant (26) and its good compatibility with silicon-based optoelectronics^[18, 19], it has potential applications as an optical coating material^[20] and as luminescent layers. Recently, violet/blue luminescence from the CeO_x film^[21] and CeO_2 film^[22] has been reported. Europium and Samarium doped Ceria thin films have been reported to give luminescence^[23] under excitation of UV light by charge transfer transition and subsequent energy transfer to Eu^{3+} . In contrast to rare-earth (RE) doped oxide phosphors



like as $\text{Y}_2\text{O}_3:\text{Eu}$ ^[24], $\text{SrTiO}_3:\text{Pr}$ ^[25] or $\text{ZnGa}_2\text{O}_4:\text{Eu}$ ^[26], few studies have been reported on luminescence of CeO_2 doped with rare-earth ions.

Tetravalent Cerium ions (Ce^{4+}) have no 4 *f* electron. This implies that CeO_2 can be a promising photoluminescence host material because of strong light absorption through the charge transfer [CT] from O^{2-} to Ce^{4+} ^[23]. If the energy transfer is achieved from the charge transfer state of CeO_2 to the doped rare earth ions, characteristic emissions are expected to be observed e. g. energy absorbed by the charge transfer from O^{2-} valence band to Ce^{4+} conduction band is transferred to the Eu^{3+} and produces the red emission. Under such a hypothesis, rare earth doped Sr_2CeO_4 materials have already been demonstrated to exhibit excellent luminescent properties ^[27]. Undoped Sr_2CeO_4 gives unusual emission in blue region. The emission was assigned to a ligands-to-metal charge transfer transition of Ce^{4+} ^[28, 29]. An efficient energy transfer can occur from the $\text{Ce}^{4+} \rightarrow \text{O}^{2-}$ charge transfer state to the trivalent RE in $\text{Sr}_2\text{CeO}_4:\text{RE}^{3+}$ (RE stands for rare earth elements) ^[30].

Raman, X-ray ^[31], XPS ^[32] of $\text{Ce}_x\text{Ln}_{1-x}\text{O}_{1-y}$, optical reflectivity ^[33] and electronic structures ^[29] of CeO_2 have been studied a lot in past but there is lack of an extensive investigation on the photoluminescence properties of $\text{CeO}_2:\text{RE}^{3+}$, especially a clear clarification of the luminescent mechanisms of $\text{CeO}_2:\text{RE}^{3+}$. The luminescent properties of undoped and rare earth doped Ceria seems to depend on the preparation method.

The photoluminescence spectra of CeO_2 nano rods showing unusual light emission at 370 nm, has been reportedly assigned to the charge transfer transition from the localized 4*f* state of Cerium to the 2*p* valence band of Oxygen ^[34]. The charge transfer emission is independent of the morphology of the sample and so it should occur in bulk CeO_2 also. However, no emission is generally observed for bulk CeO_2 . It is besides, well-known that certain oxides, like SnO_2 , ZrO_2 , CaO , or silica, show efficient defect luminescence ^[35, 36]. Hence the emission in CeO_2 nanorods may come from the deficiency of oxygen. The reported excitation wavelength of $\text{CeO}_2:\text{Eu}$ made using solid state reaction lies at 373 nm, while it occurs at 340 nm in $\text{CeO}_2:\text{Eu}$ prepared by the Pechini sol-gel process ^[37, 38].

In both the cases, the nature of excitation spectrum has been attributed to charge transfer transition from O^{2-} to Ce^{4+} and the nature of emission spectrum to defects like oxygen vacancy and symmetry distortion. Eu^{3+} emission is affected by defect and Ce^{3+} concentration in $CeO_2:Eu$ synthesized by Wet chemical method [12]. However, characteristic Eu^{3+} emission has not been observed for nanocrystals prepared by nonhydrolytic solution route [39].

4.2 Synthesis of Samples

The samples of Cerium oxide doped with rare earth activators like Europium and Terbium were synthesized by different routes viz.

1. Ceramic method (Solid State synthesis)
2. Solution Combustion method
 - I. Furnace Combustion
 - II. Microwave induced combustion
3. Co-Precipitation Method

Cerrous nitrate hexahydrate ($Ce(NO_3)_3 \cdot 6H_2O$, 99.9% purity) of Loba chemicals, Europium Nitrate Hexahydrate ($Eu(NO_3)_3 \cdot 6H_2O$, 99.9% purity) & Terbium Nitrate Hydrate ($Tb(NO_3)_3 \cdot XH_2O$, 99.9% purity) of Alfa Aesar and Urea (NH_2CONH_2 , 99% purity) of Qualigens, were used as the precursor materials.

For the synthesis of Ceria by Solid State reaction method, 5 grams of Cerium nitrate was mixed with Europium/Terbium as nitrates in stoichiometric proportion for a 2 mole percent incorporation. A minimum amount of water was added and the contents were mixed thoroughly in agate mortar and pestle. The resulting paste was transferred into silica crucible and heated at $1100^\circ C$ for 4 hours. The obtained product was a dense cake which was crushed and grinded to fine powder with mortar and pestle. The powder was washed with acetone to remove the residual impurities like nitrate ions. The final product obtained was light yellow coloured powder.

For synthesis by Furnace combustion method, 5 grams of Cerium Nitrate (*oxidizer*) and 2 mole percent equivalent of Europium/Terbium as nitrates was mixed with varying

amounts of Urea (fuel) for Stoichiometric (2.5), fuel rich (3.0) and fuel deficient ratios (2.0) in a 250 ml Schott Duran (Germany) Round Bottom flask. The corresponding equivalence ratio ϕ_e (discussed in chapter 3) was calculated and found to be 1.0 for stoichiometric, 0.88 for fuel rich and 1.16 for fuel lean ratios. The amount of water added to the mixture was about 0.667 ml/gm of nitrate [ni]. It was heated at moderate rate with stirring for 30 minutes to allow homogenous mixing of the constituents. The mixture was then introduced into a muffle furnace preheated at around 500°C. Initially the mixture starts boiling and slowly the water gets evaporated. The solution (paste) melts (boils) and undergoes dehydration followed by decomposition with the evolution of large amounts of gases (oxides of nitrogen and ammonia). The redox mixture is then auto ignited resulting in an exothermic reaction with a flame producing a sound with the flame temperature above 1100°C. The reaction was violent and vigorous and the products flew out of the container during the process. Dark yellow coloured residue chunks were obtained which were voluminous, porous and foamy in nature. These chunks were grinded with mortar and pestle to obtain fine powder which was then washed with acetone to remove the residual impurities. The final product was dark yellow coloured fine powder.

In case of Microwave combustion synthesis, the above mentioned mixtures were taken in a 250 ml Schott Duran (Germany) round bottom flask and placed inside a modified kitchen microwave oven (discussed in chapter 3) with output power of 850 watts and frequency of 2.45 GHz for a few minutes. During this time, the redox mixture boiled with the evolution of large amount of gas, underwent dehydration and ignited (due to internal heating) resulting in an exothermic reaction with a flame releasing large amount of heat and producing a sound. Here also a dark yellow coloured residue was obtained which was voluminous, porous and foamy in nature. The powder was washed with acetone to remove the residual impurities and grinded with mortar and pestle. The final product was dark yellow coloured fine powder.

In Co-precipitation method, 3.249 gram of $\text{Ce}(\text{NO}_3)_3$ was dissolved in 50 ml of alcohol to obtained 0.2 mol/liter solution. This solution was added dropwise into an alcoholic

solution of 2 mol/liter ammonium hydroxide at the rate of 4 ml/minute and vigorously stirred. The temperature was maintained at 50° C. As the precipitation occurred, the final pH of the solution was greater than 9. These precipitates were filtered and washed with acetone several times to get rid of residual impurities. The precipitates were dried in a vacuum desiccators for 10-12 hours and finally dried in an oven at 100°C for 12 h. Ferric Hydroxide nanoparticles were obtained. These nanoparticles were calcined at 600° C for 2 hours to obtain the Ferric Oxide nanoparticles. The powders thus obtained were collected in glass bottles.

4.3 Characterization of Samples

These samples were characterized by X-ray diffraction (XRD). They were further investigated by Scanning electron microscopy (SEM). Their Fluorescence and UV-Visible characteristics were also studied.

X - Ray Diffraction

The XRD patterns were taken of Bruker D8 advance X-ray diffractometer. The 2θ range was taken from 20° to 100° in scan mode with step increment of 0.050° and step time 2 seconds at room temperature. The XRD patterns are given in Figures C_x 1 to C_x 9. The XRD of commercially available sample is also given for reference.

Reflections for sample C1 show very sharp features with high intensity. Ten prominent peaks are observed. The pattern indicates the high degree of crystallinity of the sample. The peak at 2θ value of 28.571° has the highest intensity followed by 47.511° and 56.375°. d values of all the peaks match very closely with those reported in JCPDS file number 4-0593. The lattice constant for (111) plane is 0.540678 nm.

Reflections for Sample C2 again show very sharp features with high intensity. There are 10 peaks observed and the reflection at 2θ value of 28.576° has the highest intensity followed by 47.513° and 56.369°. The broadening of peaks is observed to be minimum. d values of all the peaks match very closely with those reported in JCPDS file number 4-

0593. These d values also match very closely to the reflections of the commercially available CeO₂ shown in figure C_x 1. The lattice constant for (111) plane is calculated to be 0.540585 nm.

XRD of Sample C1

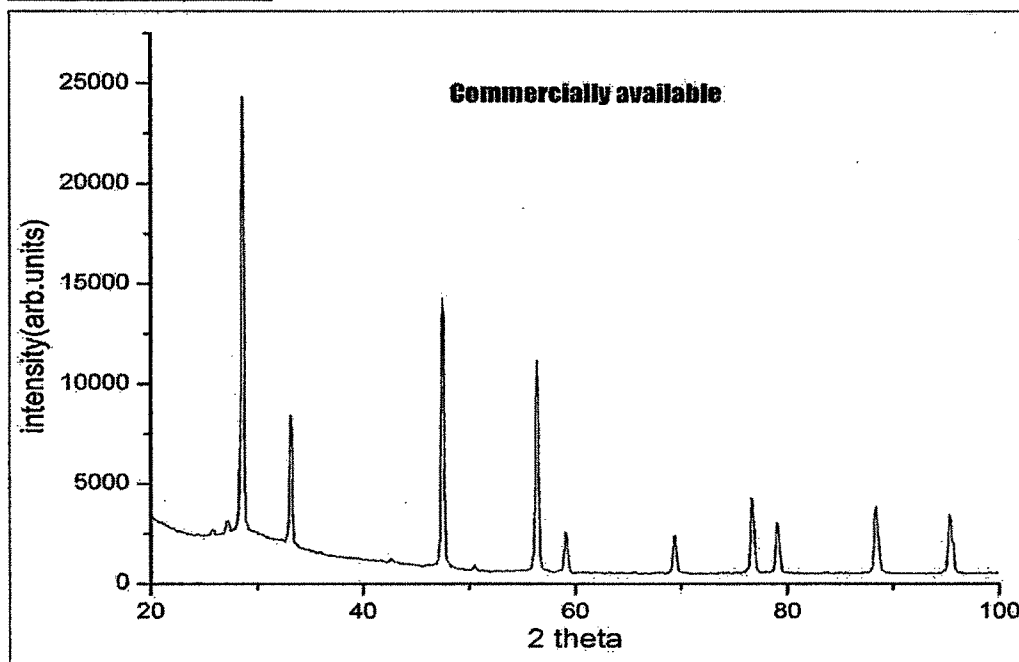
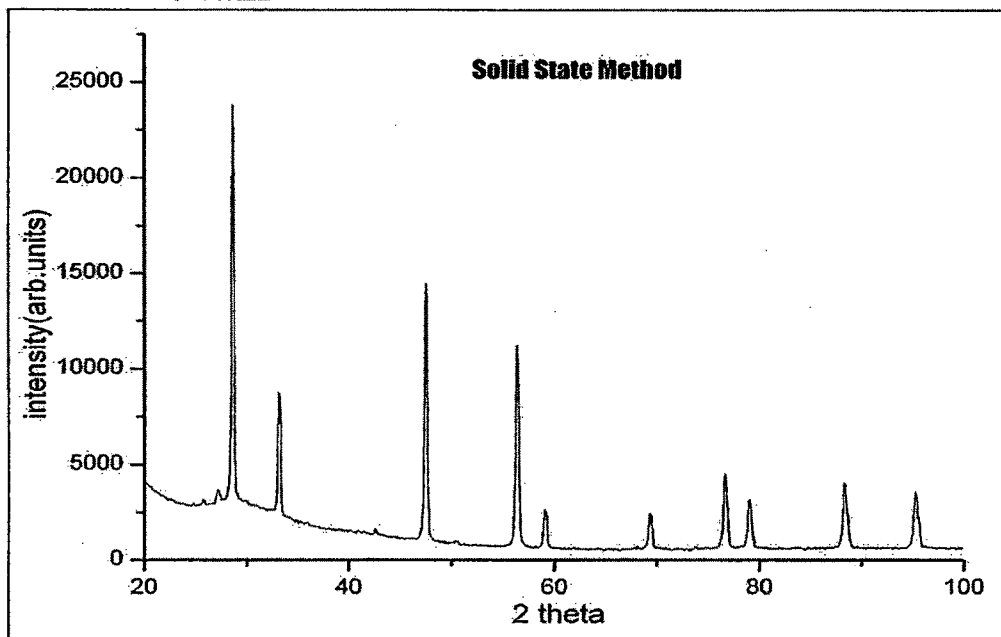
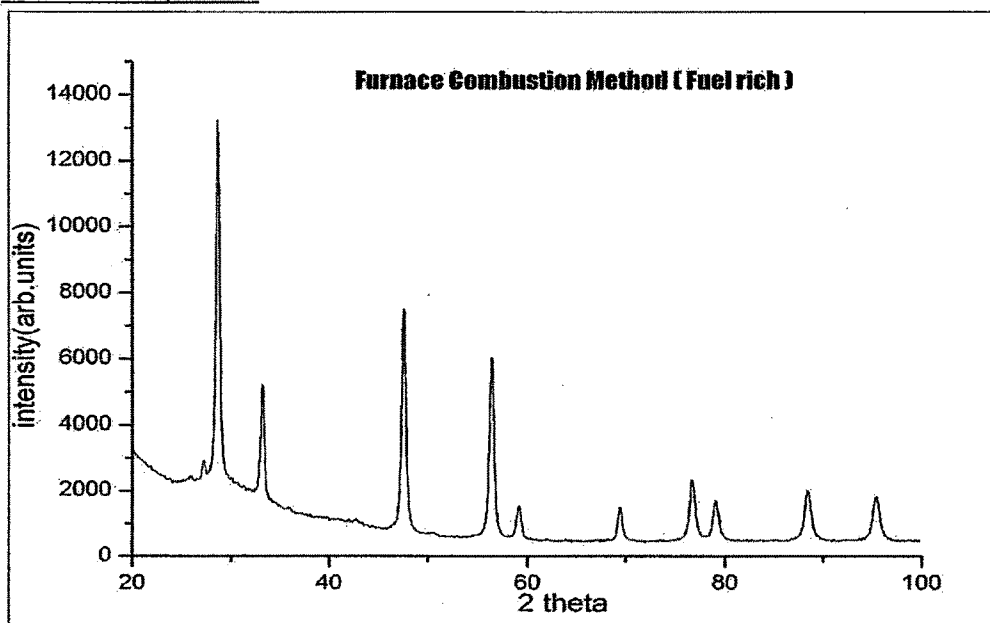
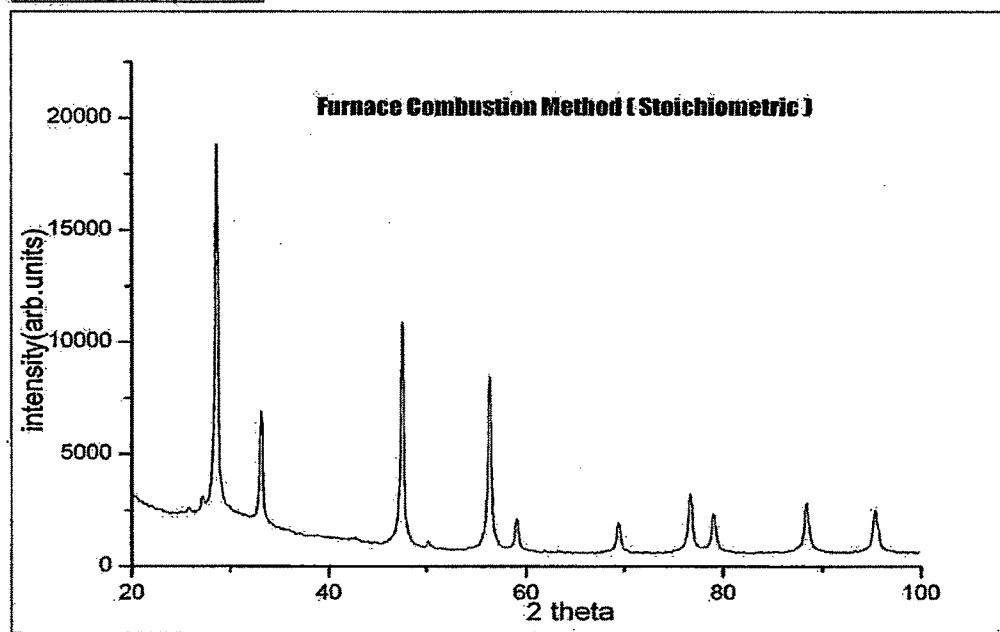


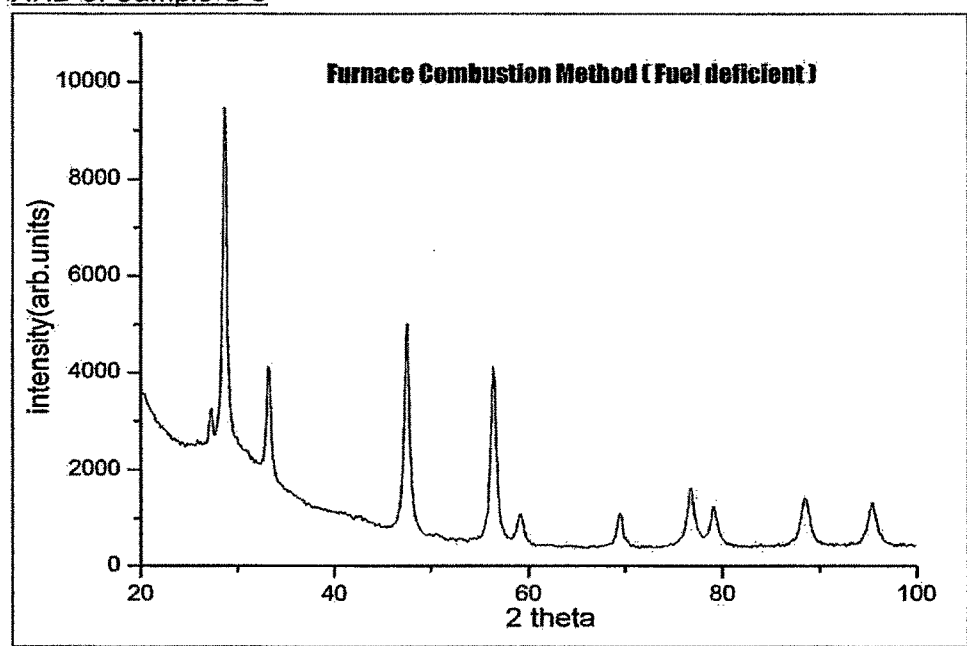
Figure C_x 1

XRD of Sample C 2Figure C_x 2XRD of Sample C 3Figure C_x 3

XRD of Sample C 4

Figure C_x 4

XRD of Sample C 5

Figure C_x 5

XRD of Sample C 6

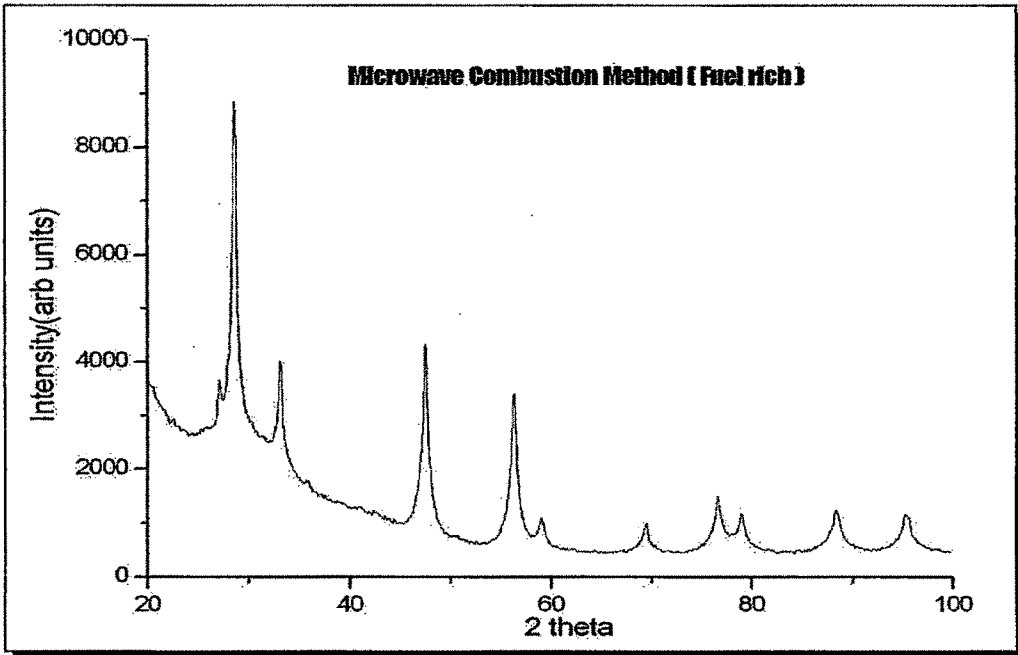


Figure C_x 6

XRD of Sample C 7

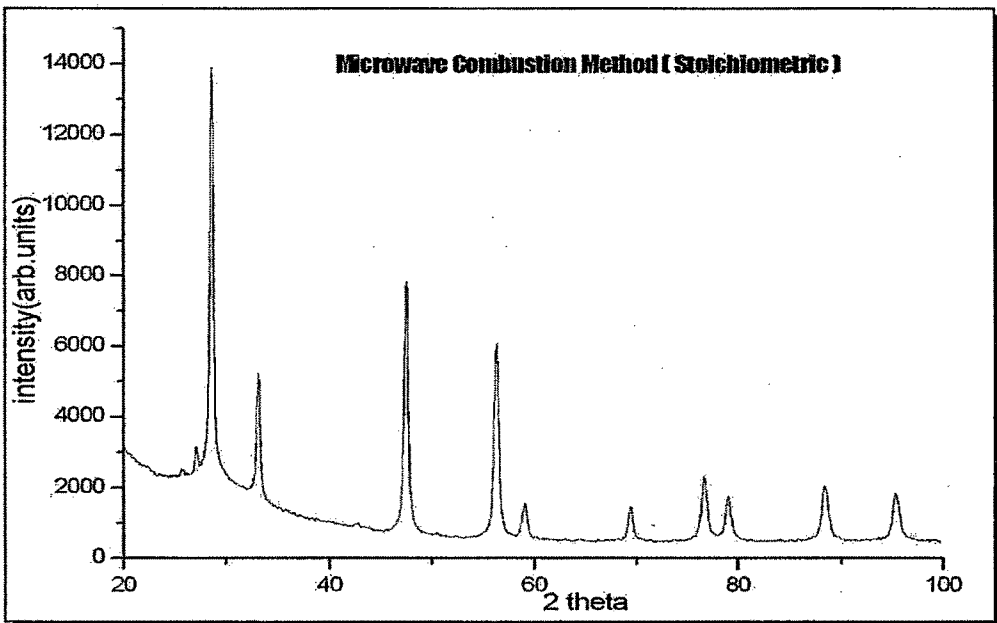
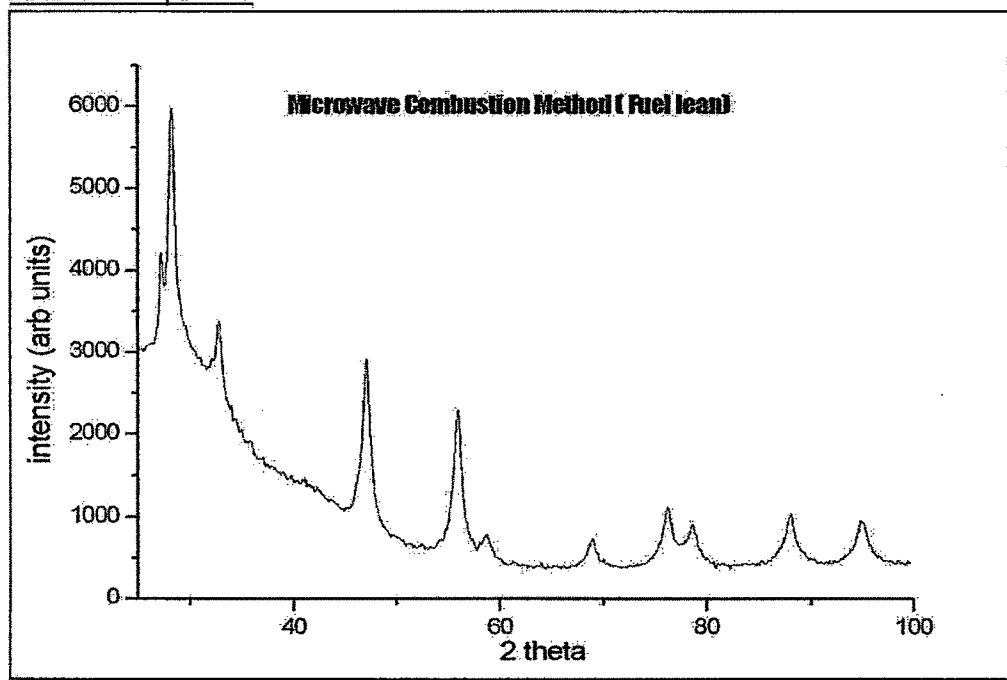
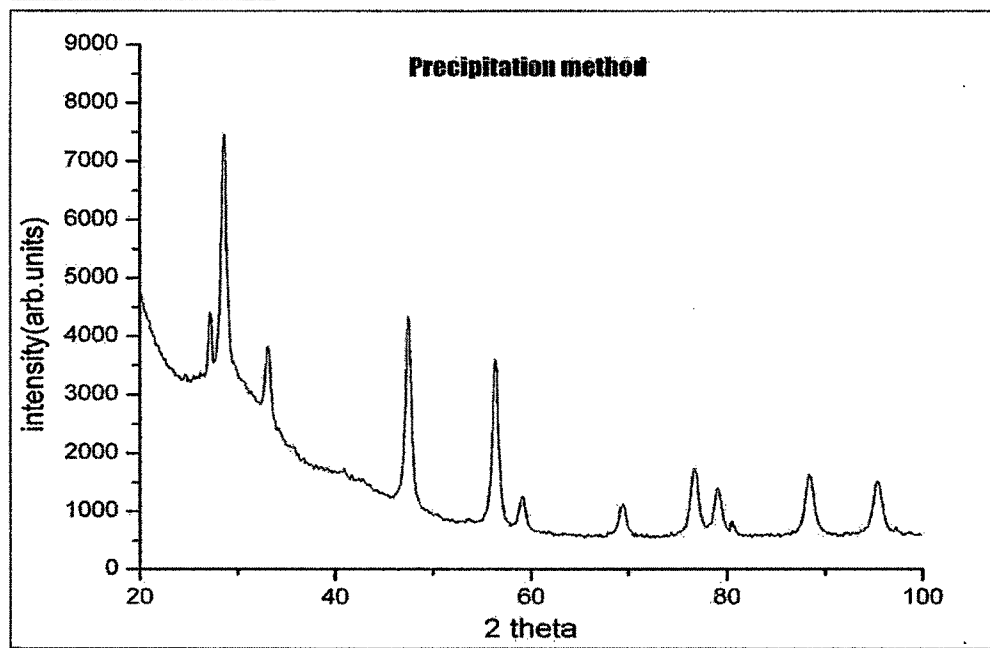


Figure C_x 7

XRD of Sample C 8

Figure C_x 8

XRD of Sample C 9

Figure C_x 9

Reflections for Sample C3 follow the same trend. The reflection at 2θ value of 28.606° has the highest intensity followed by 47.554° and 56.416° . The intensities of the peaks are less compared to the intensities of the peaks for Sample C1 and C2. Some amount of broadening is observed which is higher than for samples C1 and C2. d values of all the peaks match closely with those reported in JCPDS file number 4-0593. These d values match closely to the reflections of the commercially available CeO_2 given in figure C_x 1. The lattice constant for (111) plane is 0.540036 nm and the corresponding crystallite size is found to be 18.9602 nm.

Reflections for Sample C4 are seen to be similar. The reflection at 2θ value of 28.571° has the highest intensity followed by 47.505° and 56.365° . Here also, the intensities of the peaks are less compared to the intensities of the peaks for Sample C1 and C2 but more than Sample C3. Some amount of broadening is observed which is higher than for samples C1 and C2 but is less than sample C3. d values of all the peaks match closely with those reported in JCPDS file number 4-0593. These d values match very closely to the reflections of the commercially available CeO_2 in figure C_x 1 compared to other samples. The lattice constant for (111) plane is calculated to be 0.540678 nm and the corresponding crystallite size is found to be 24.0576 nm.

Reflections for Sample C5 show sharp features with high intensity but less sharper than samples C1, C2, C3, C4. Same number of peaks is observed and the reflection at 2θ value of 28.611° has the highest intensity followed by 47.548° and 56.406° . The intensities of the peaks are less compared to the intensities of the peaks for Sample C1, C2, C3 and C4. The broadening observed is higher than for samples C1, C2, C3 and C4. d values of all the peaks match closely with those reported in JCPDS file number 4-0593. The d values match closely to the reflections of the samples C1, C2, C3. However, there is some deviation observed when compared to sample C4. The lattice constant for (111) plane is calculated to be 0.539937 nm and the corresponding crystallite size is found to be 15.9704 nm.

Reflections for Sample C6 show sharp features with good intensity but less sharper than samples C1, C2, C3, C4 and more sharper than sample C5. The reflection at 2θ value of 28.580° has the highest intensity followed by 47.508° and 56.371° . The broadening

observed is higher than for samples C1, C2, C3 and C4 but relatively less than sample C5. d values of all the peaks of sample match closely with those reported in JCPDS file number 4-0593. The d values of sample C6 match more closely to the reflections of the samples C1, C2, C3, C4 compared to sample C5. The lattice constant for (111) plane is calculated as 0.540514 nm and the corresponding crystallite size is found to be 16.0381 nm.

Reflections for Sample C7 show sharp features with good intensity but less sharper than samples C1, C2, C3, C4 and more sharper than sample C5, C6. The reflection at 2θ value of 28.565° has the highest intensity followed by 47.500° and 56.362° . The broadening observed is higher than for samples C1, C2, C4, is comparable to sample C3 but relatively less than sample C5 and C6. d values of all the peaks of sample closely match with those reported in JCPDS file number 4-0593. The d values of sample C7 match more closely to the reflections of the sample C1, C2, C3, C4 compared to samples C5 and C6. The lattice constant for (111) plane is calculated as 0.540794 nm and the corresponding crystallite size is found to be 19.5391 nm.

Reflections for Sample C8 show sharp features with reasonably good intensity. The reflection at 2θ value of 28.175° has the highest intensity followed by 32.673° and 47.074° . The intensities of the peaks are less compared to the intensities of the peaks for all previous samples. The broadening observed is quite pronounced and higher than for samples C1, C2, C3, C4, C5, C6 and C7. The d values of sample C8 deviate slightly from those of other samples, as also the relative intensities, which can be distinctly observed in Figure C_x10. However, it is in close conformity with the JCPDS values. The lattice constant for (111) plane is calculated as 0.548133 nm and the corresponding crystallite size is found to be 13.4471 nm.

Reflections for Sample C9 show sharp features with reasonably good intensity. The reflection at 2θ value of 28.579° has the highest intensity followed by 47.526° and 56.392° . The intensities of the peaks are less compared to the intensities of the peaks for Sample C1, C2, C3, C4, C5, C6, C7 but relatively more than sample C8.

JCPDS File No. 4-0593	C1	C2	C3	C4	C5	C6	C7	C8	C9
3.124	3.12170	3.12116	3.11799	3.12170	3.11742	3.12075	3.12150	3.11739	3.12084
2.706	2.70407	2.70439	2.70130	2.70428	2.70187	2.70378	2.70436	2.69633	2.70325
1.913	1.91219	1.91211	1.91059	1.91244	1.91080	1.91231	1.91248	1.91424	1.91161
1.632	1.63076	1.63091	1.62966	1.63101	1.62992	1.63087	1.63108	1.63421	1.63029
1.562	1.56136	1.56155	1.56047	1.56187	1.56062	1.56187	1.56157	1.56631	1.56052
1.353	1.35259	1.35259	1.35176	1.35270	1.35147	1.35219	1.35258	1.35242	1.35069
1.241	1.24106	1.24140	1.24038	1.24128	1.24029	1.24113	1.24118	1.24303	1.24003
1.210	1.20980	1.21008	1.20896	1.20993	1.20890	1.20971	1.20983	1.21206	1.20949
1.1044	1.10451	1.10467	1.10381	1.10464	1.10370	1.10428	1.10439	1.10614	1.10373
1.0412	1.04127	1.04152	1.04080	1.04148	1.04072	1.04188	1.04143	1.04296	1.04050

Table 1: d values of samples

The broadening observed is quite pronounced and higher than for samples C1, C2, C3, C4, C5, C6, C7 but less than sample C8. d values of all the peaks of samples closely match with those reported in JCPDS file number 4-0593. The d values of sample C9 match more closely to the reflections of the sample C1, C2, C3, C4, C5, C6, C7 than sample C8 but the deviation is quite high. The lattice constant for (111) plane is calculated as 0.540529 nm and the corresponding crystallite size is found to be 13.0481nm which is smallest compared to other samples.

The patterns show sharp features with high intensity thus indicating the crystallinity of the samples, except for the samples prepared by microwave combustion in fuel lean ratio and precipitation methods, which have peaks with lower intensities.

The d values match almost exactly with the standard values given in JCPDS file number 4-0593 for Ceric Oxide (Cerianite). This sample also shows a deviation in the trend of relative intensities observed for the other samples. The d values are given in **Table 1**.

All the X ray reflection peaks of the XRD patterns given from figures C_x 1 to C_x 9 could be easily indexed with the reported values in the JCPDS file of Cerium oxide (Cerianite) precisely. This confirms the formation of CaF₂ type FCC cubic fluorite unit cell with the space group Fm3m. The structural parameters like lattice constant and lattice volume are given in **Table 2**.

Good amount of broadening in the peaks is observed for samples synthesized by Combustion method and Co- precipitation method compared to sample synthesized by Solid state method and the commercially available sample. From the broadening of the peaks, size of crystallites can be calculated by Scherrer formula (discussed in Chapter2). The intensities of all the peaks in all the diffraction patterns follow a regular pattern as shown in figure C_x 10.

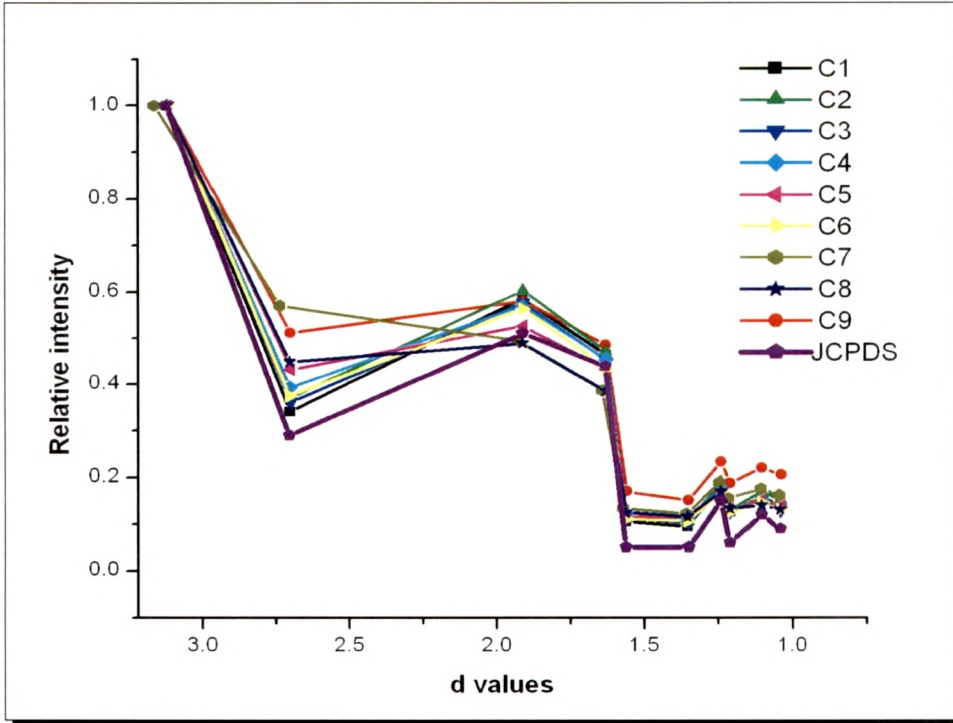
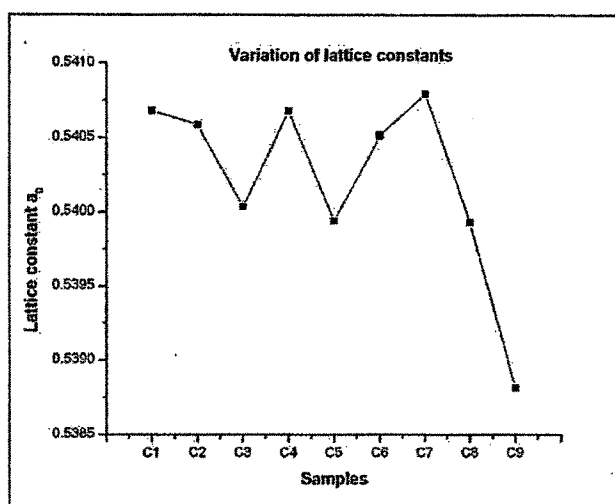


Figure C_x 10: Change in relative intensity with d values

Sample	<i>d</i> spacing nm	Lattice constant <i>a</i> ₀ nm	Cell Volume <i>V</i> = <i>a</i> ₀ ³
C9	0.311084	0.538813	0.156428
C8	0.311739	0.539929	0.157394
C7	0.312237	0.540794	0.158160
C6	0.312075	0.540514	0.157914
C5	0.311742	0.539937	0.157409
C4	0.312170	0.540678	0.158058
C3	0.311799	0.540036	0.157495
C2	0.312116	0.540585	0.157976
C1	0.312170	0.540678	0.158058

Table 2: Lattice constant and cell volume [(111) plane]



The figure above shows the variation in lattice constants for the prepared samples. It is interesting to note that the minimum value is for the sample synthesized by co-precipitation method, which has the smallest particle size. It indicates the effect of size reduction on the lattice constant. The reduced particle size leads to higher internal strain which is the most probable reason for shrinking of the lattice parameter. The samples with stoichiometric proportions (C1, C2, C4 and C7) have lattice constants of the same order. It needs to be mentioned here that for the commercially available and solid state samples, the reactants are in stoichiometric proportions.

The crystallite size of the samples for the respective planes and their average, calculated by Scherrer formula is given in tables below. This sizes are calculated after subtracting the instrumental broadening from the samples by using X ray diffraction pattern of silicon as a reference as described in Chapter 2. The crystallite size of the samples for the respective planes and their average, calculated by Scherrer formula is given in **Tables** below.

This sizes are calculated after subtracting the instrumental broadening from the samples by using X ray diffraction pattern of silicon as a reference as described in Chapter 2. There is always some amount of strain present in the crystals as their size decreases. This strain also causes broadening of peaks. This broadening has to be numerically removed to get actual crystal size. Crystallite sizes after deducting the strain factor can be

calculated by a graphical method, as discussed in Chapter 2. The graphs are given below. A typical data for determining crystal size by removing the strain is given in **Table 3**.

It is found that there is significant increase in crystal size as the strain is removed. The strain is found to be minimum in samples synthesized by Co – precipitation method. It is found to be maximum in samples synthesized by microwave and furnace combustion method with stoichiometric ratios followed by fuel rich and fuel lean ratios. During the process of combustion with stoichiometric ratio, the flame temperature is highest. The rapid combustion and quenching of reaction from very high temperature to room temperature induces additional surface and bulk defects [1] which may be the cause of strain in the samples.

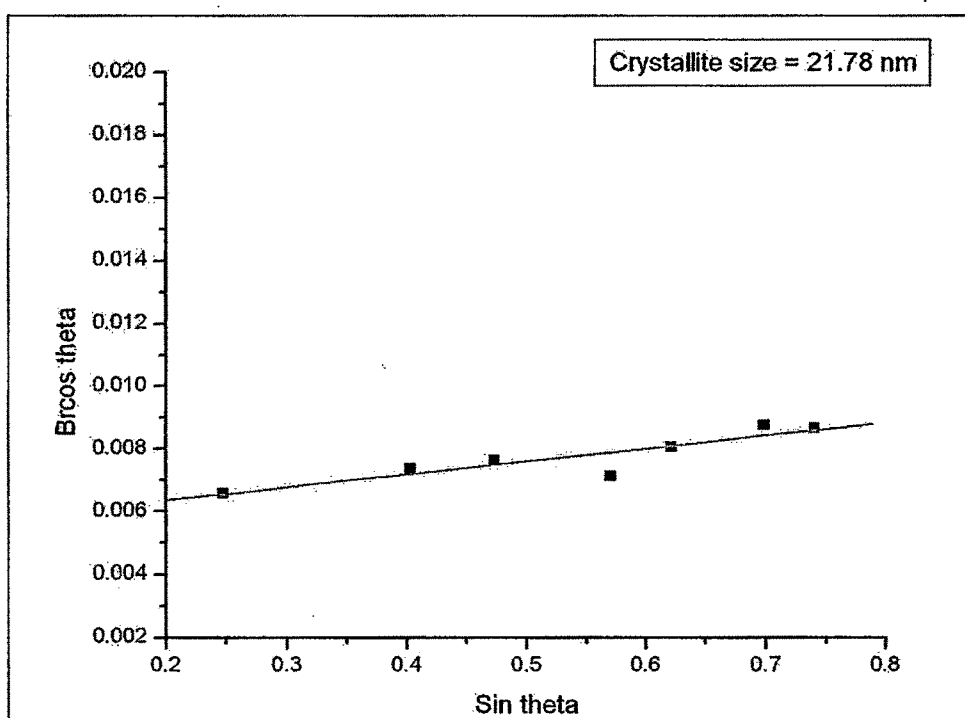
2θ values	FWHM	Silicon 2θ values	Silicon FWHM	B_i^2	B_o^2	$B_r = \sqrt{B_o^2 - B_i^2}$	$\sin \theta$	$B_r \times \cos \theta$
28.579	0.590	28.370	0.1145	3.993×10^{-6}	0.000106	0.01010	0.24682	0.00978
47.526	0.654	47.238	0.1096	3.659×10^{-6}	0.000130	0.01125	0.40295	0.01029
56.392	0.668	56.060	0.1076	3.526×10^{-6}	0.000135	0.01150	0.47248	0.01014
69.543	0.725	69.078	0.1135	3.924×10^{-6}	0.000160	0.01249	0.57030	0.01026
76.807	0.789	76.322	0.1090	3.619×10^{-6}	0.000189	0.01363	0.62119	0.01068
88.519	0.952	87.981	0.1208	4.445×10^{-6}	0.000276	0.016481	0.697909	0.01180
95.517	0.991	94.903	0.1290	5.069×10^{-6}	0.000299	0.017149	0.740318	0.01152

Table 3: Data for determination of crystallite size by graphical method for a typical sample (prepared by co-precipitation method)

Sample C3

Crystallite size by Sherrer Formula

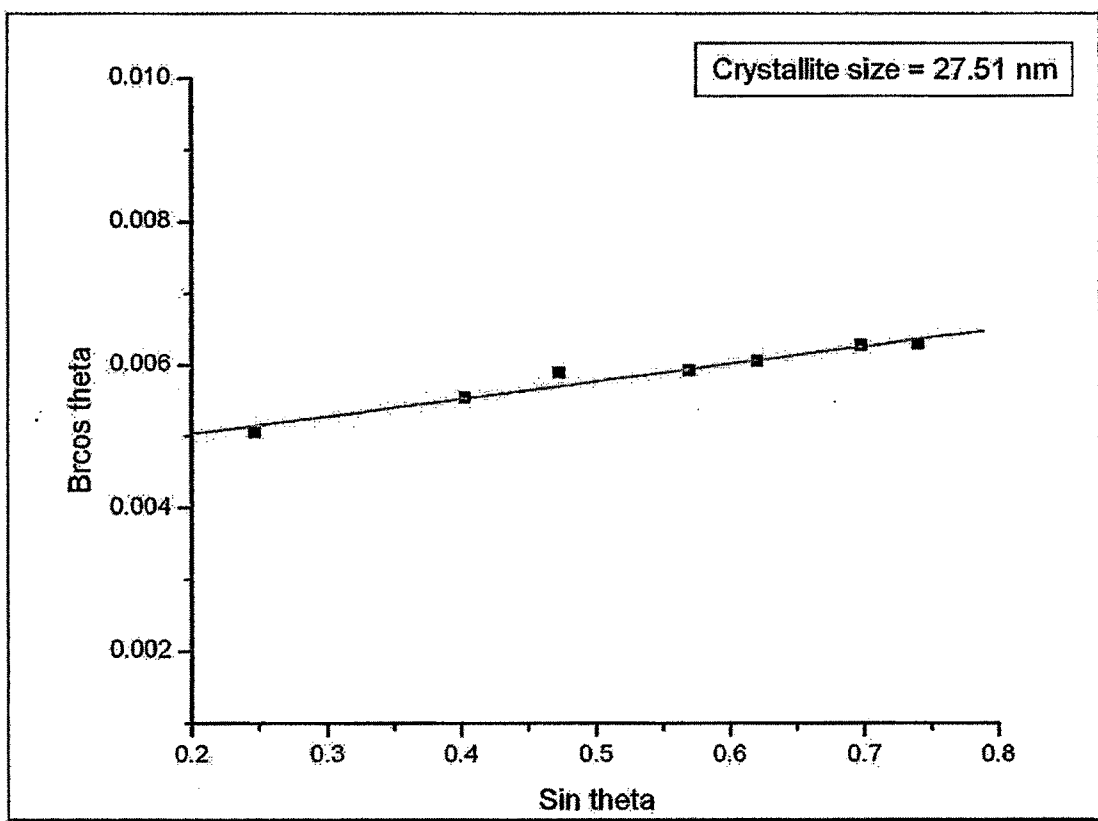
d values(°A)	Crystallite Size (nm)
3.11799	18.9602
2.70130	19.4241
1.91059	15.3371
1.62966	13.7537
1.56047	12.8654
1.35176	12.8001
1.24038	10.3949
1.20896	9.07477
1.10381	8.59942
1.04080	7.13266
Average Crystallite Size	12.83 nm



Sample C4

Crystallite Size by Scherrer Formula

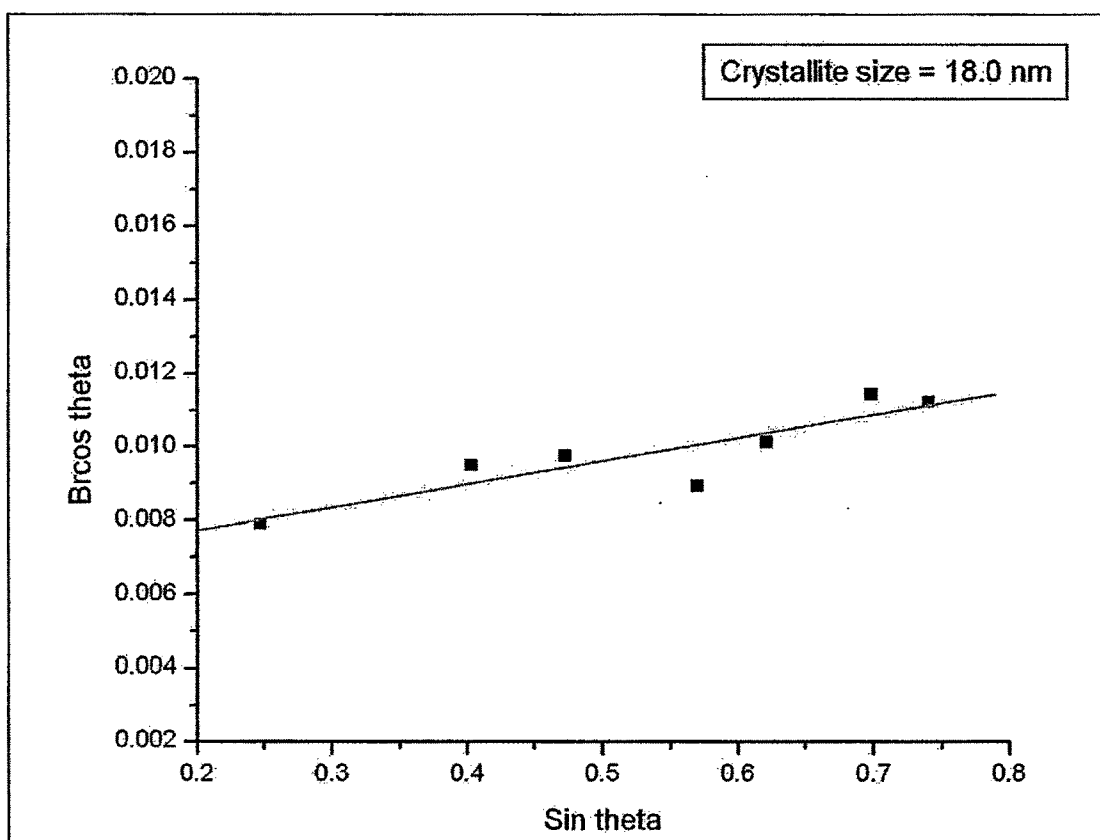
d values (°A)	Crystallite Size (nm)
3.12170	24.0576
2.70428	23.7227
1.91244	19.9757
1.63101	17.5937
1.56187	17.9967
1.35270	15.2576
1.24128	13.6609
1.20993	13.5834
1.10464	11.0348
1.04148	9.70339
Average Crystallite Size	16.66 nm



Sample C5

Crystallite Size by Scherrer Formula

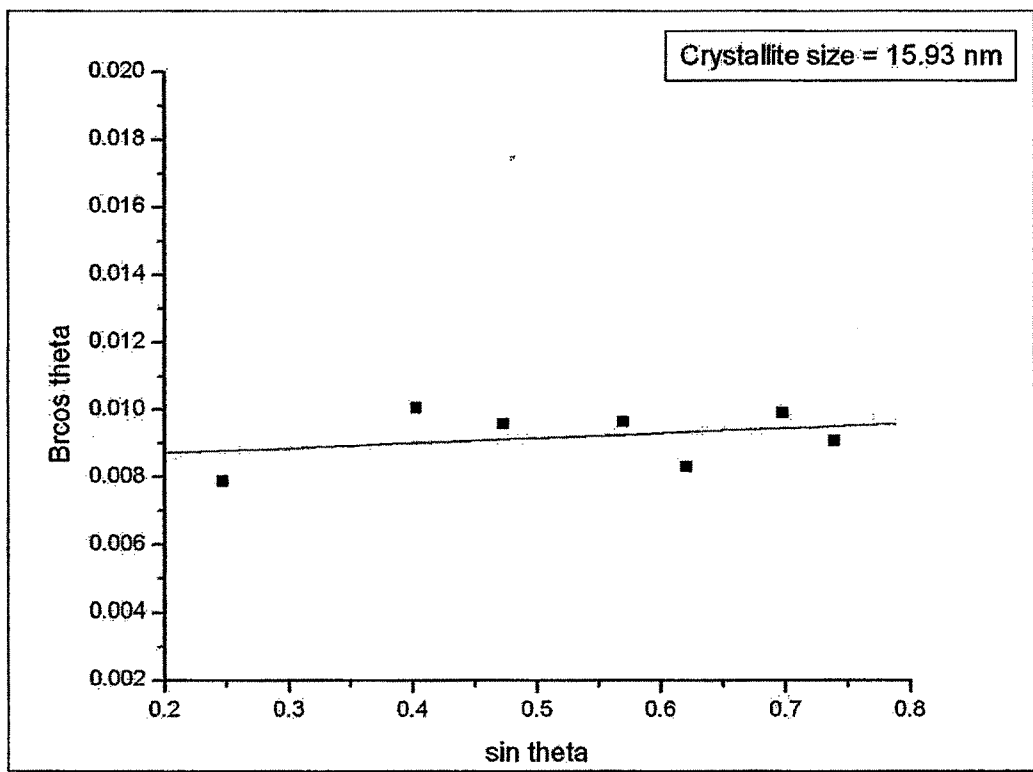
d values (°A)	Crystallite Size (nm)
3.11742	15.9704
2.70187	16.6617
1.91080	12.0165
1.62992	10.871
1.56062	10.5159
1.35147	10.2955
1.24029	8.31274
1.20890	8.69683
1.10370	6.16397
1.04072	5.5356
Average Crystallite Size	10.50 nm



Sample C6

Crystallite size by Scherrer Form

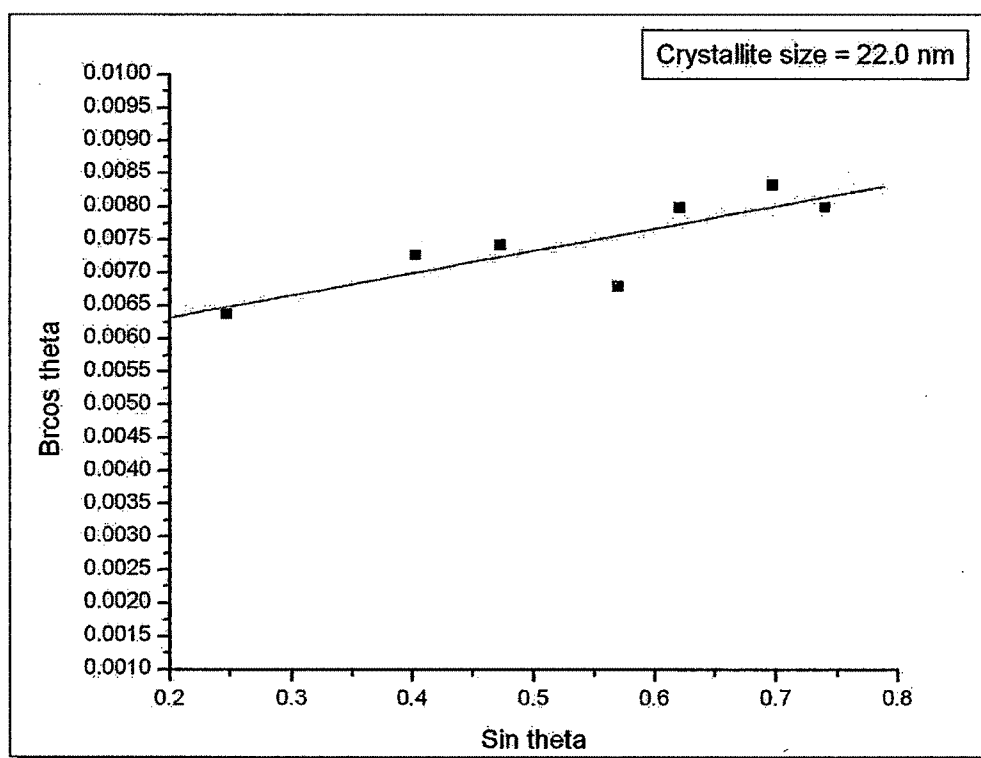
d values (°A)	Crystallite Size (nm)
3.12075	16.0381 nm
2.70378	16.8099 nm
1.91231	11.3789 nm
1.63087	11.0793 nm
1.56187	11.9978 nm
1.35219	9.58744 nm
1.24113	10.0955 nm
1.20971	9.57086 nm
1.10428	7.10631 nm
1.04188	6.83146 nm
Average Crystallite Size	11.05 nm



Sample C7

Crystallite size by Scherrer Formula

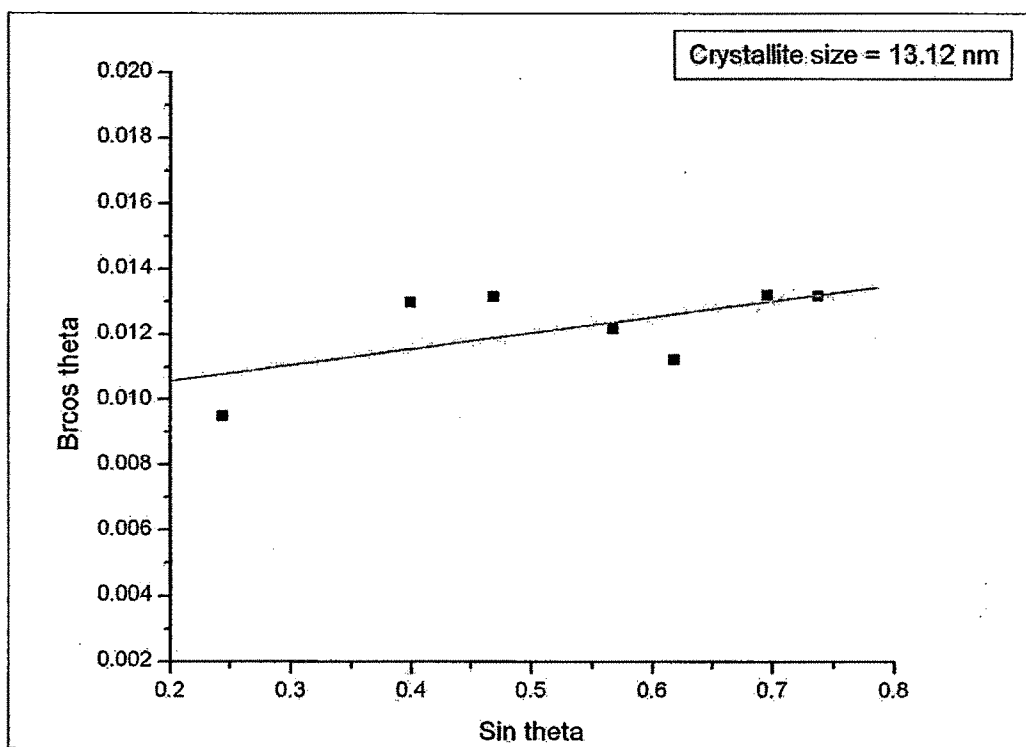
d values (°A)	Crystallite Size (nm)
3.12150	19.5391
2.70436	19.426
1.91248	15.5367
1.63108	14.1748
1.56157	13.3921
1.35258	13.4085
1.24118	10.4867
1.20983	10.8805
1.10439	8.40869
1.04143	7.71466
Average Crystallite Size	13.30 nm



Sample C8

Crystallite size by Scherrer Formula

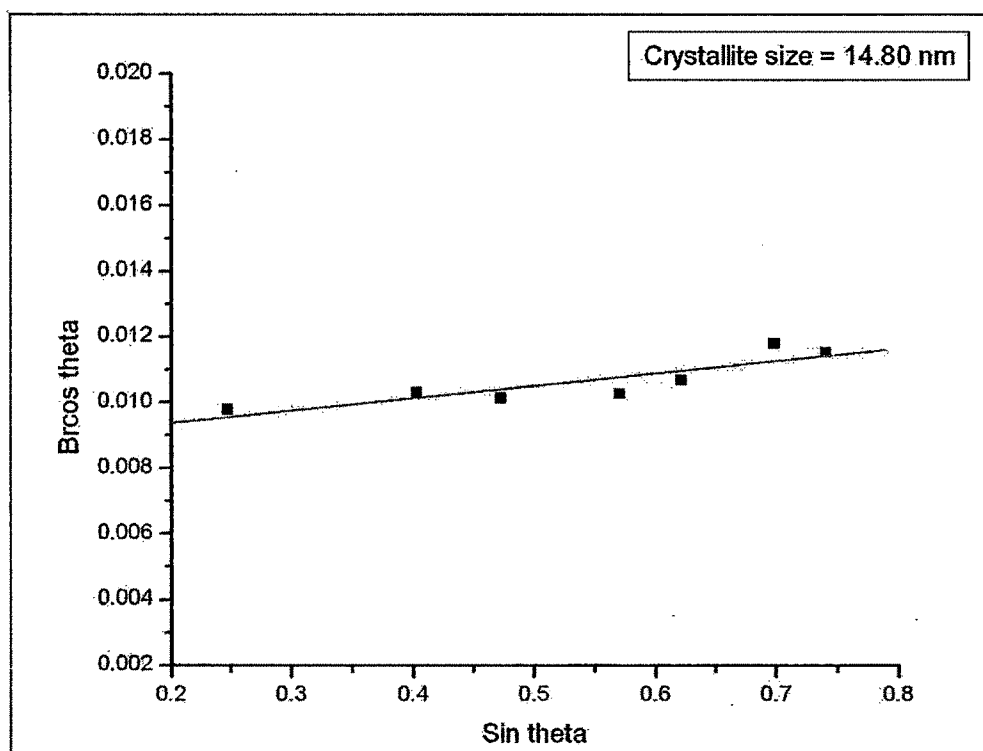
d values (°A)	Crystallite Size (nm)
3.16474	13.4471
2.73858	15.6537
1.92894	8.89274
1.64268	8.1587
1.57039	
1.35844	7.65313
1.24619	7.56013
1.21455	7.84414
1.10733	5.38394
1.04498	4.77586
Average Crystallite Size	8.82 nm



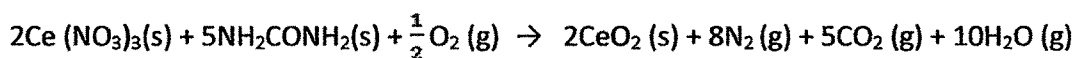
Sample C9

Crystallite Size by Scherrer Formula

d values (°A)	Crystallite Size (nm)
3.12084	13.0481
2.70325	12.7559
1.91161	11.117
1.63029	10.4811
1.56052	11.7304
1.35069	9.00379
1.24003	7.89065
1.20949	8.1859
1.10373	5.9758
1.04050	5.38912
Average Crystallite Size	9.56 nm



The reaction between Cerrous nitrate ($\text{Ce}(\text{NO}_3)_3 \cdot 6\text{H}_2\text{O}$) and urea is highly exothermic and self propogating in nature. It is given by;



The reaction becomes very vigorous and violent and bursting sound is heard. The product flew out of container. Formation of CeO_2 from Cerous nitrate urea redox mixture requires atmospheric oxygen for the oxidation of Ce^{3+} to Ce^{4+} during combustion. 11.5 moles of gases are released per mole of CeO_2 when the fuel and oxidizer are mixed stoichiometrically. Thermochemical calculations reveal that the heat of combustion of Cerous nitrate redox mixtures is very high ^[40]. This is the reason for the reaction becoming vigorous and violent. Highest flame temperature is attained in stoichometric ratio compared to fuel lean and fuel rich ratios. The complete decomposition of Cerium nitrate to CeO_2 occurs below 350°C ^[41]. Since the flame temperature is higher than decomposition temperature auto ignition of the respective constituents produces CeO_2 .

Urea on heating is reported ^[42, 43] to decompose to biuret and ammonia initially and at higher temperatures to $(\text{HNCO})_3$ trimer. On the other hand, $\text{Ce}(\text{NO}_3)_3 \cdot 6\text{H}_2\text{O}$ ^[44] melts on heating followed by dehydration and decomposition to amorphous ceria and oxides of nitrogen. Thus, during the combustion of Cerous nitrate - Urea mixture, all these reactions appear to occur simultaneously forming a polymeric gel which foams due to the large amounts of gases produced ^[43]. The appearance of a flame may be attributed to the gas phase reactions in the form of combustible gases like ammonia and cyanic acid with oxides of nitrogen. Ammonia-nitrogen oxide flames are known ^[44, 45] to give a flame having a temperature of $\approx 2000^\circ\text{C}$. Thus, production of high temperatures ($>1100^\circ\text{C}$) during the combustion of Cerous nitrate - Urea mixtures during the process of reaction is a certainty, though the temperatures were not measured.

In general, for the combustion synthesis process of Ceria, it is observed that the average crystallite size is minimum for samples with fuel lean ratio followed by

samples with fuel rich ratio and stoichiometric ratio in increasing order. High flame temperatures due to generation of heat of combustion and evolution of gases are two major events which occur during Combustion synthesis. Heat of combustion helps in crystallization and formation of the desired phase. Therefore, high flame temperature will increase the crystallite size, make the active primary particles sinter during combustion, reduce the surface area, and form a dense structure in the agglomerates. On the other hand, associated gas evolution will cool the products, reduce the possibility of premature partial sintering, prevent the further growth of crystallites and give porous structure of the powders ^[46, 47]. The gas evolution also helps in limiting the interparticle contact and hence resulting in more easily friable product with very small crystallite size. These two effects are opposite and competing. The highest flame temperature is attained for stoichiometric ratio for Cerous nitrate - Urea mixtures. As the fuel content increases the flame temperature should also increase further, subject to the availability of enough oxidant required for complete combustion of the excess fuel. However it was observed that the crystallite size decreases for fuel rich ratio compared to stoichiometric ratio. The relatively low flame temperatures are believed to be responsible for smaller crystallite sizes. Here the combustion process proceeds at slower rate and the number of moles of gases released are higher compared to stoichiometric ratio. So, these gases reduce the flame temperature, resulting in smaller crystallite size. In Fuel deficient ratio the amount of fuel available is less. Hence, incomplete decomposition of nitrates may occur ^[46]. The flame is not observed and the combustion process gets over in a very short period of time compared to other ratios with release of a large amount of gases. Thus lowest flame temperature with release of large amount of gases compared to other two ratios is responsible for smallest crystallite size obtained amongst the three ratios. The intensity of the peaks is less for the samples with fuel lean ratios which shows that their crystallinity is not good. There may be some amount of amorphicity present as the process of combustion may not be completed.

During furnace combustion process the Cerous nitrate urea mixture is introduced into a furnace which is preheated at 500°C. So the heat available before the start of self

propagating reaction is large. The heat is produced externally. Heat is generated by heating elements and then transferred to the sample surfaces and then transferred to the interior by conduction. The heat transfer is also non uniform in nature.

During the process of microwave combustion the mixture is kept in a microwave oven which is at room temperature. Then the microwave irradiates the mixture and takes it almost instantly to the temperature where combustion reaction can start and become self propagating. This duration is very short. When the reaction starts, the electromagnetic field polarizes metal nitrate water mixture which induces a dipole moment in the molecule. Hydrated water molecules have high dielectric constant and it increases the polarity of metal nitrates allowing strong microwave coupling. As a result increased rotation sets in which causes internal heating due to frictional effects ^[48]. Therefore, rapid heating takes place. Heat is generated throughout the material volume. This causes formation of oxide as a transient phase. Thus in microwave heating the heat is generated within the sample itself by interaction of microwaves with the material. There is an inverse heating profile observed here in comparison to furnace combustion ^[49, 50]. There is 100 % conversion of electromagnetic radiation into heat unlike conventional heating where there are significant thermal energy losses ^[50]. It is also found that microwave combustion processed samples ignite at lower temperatures compared to conventional furnace combustion processed samples. After the furnace combustion process is over and when the furnace is cooling down, the furnace has still some heat left inside which may cause further heating of the resultant powder whereas in microwave oven the heat available is very less.

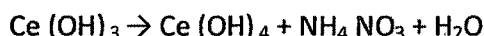
Due to all these factors the heating of Cerous nitrate urea mixtures is very rapid in microwave combustion reaction compared to furnace combustion reaction. The samples also ignite at lower temperatures leading to smaller crystallite sizes than for samples synthesized by furnace combustion method.

Samples synthesized by Solid state synthesis method have very large crystallite size. Since they are heated for a prolonged period for high temperatures (1100°C), the heat provides energy for the crystal to grow. The crystallinity is generally very high for these kinds of samples. This can be confirmed by XRD patterns with peaks of high intensity.

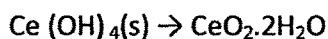
Co-precipitation reaction occurs at 50°C. The Cerous nitrate is dissolved in ethanol giving Ce^{3+} and $(\text{NO}_3)^-$ ions. The reaction mechanism is given below ^[51, 52].



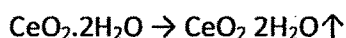
The ions undergo hydrolysis to form $\text{Ce}(\text{OH})_3$. Oxidation of $\text{Ce}(\text{OH})_3$ occurs readily to give yellow $\text{Ce}(\text{OH})_4$ precipitates.



The formation of Ceria occurs after the oxidation of Ce^{3+} to Ce^{4+} in the solution at high pH (≥ 9.5). This hydroxide precipitate is transformed into an intermediate Cerium oxide dihydrate ^[52].



Calcining of this product gives Cerium oxide nanoparticles.



The heat needed for the crystals to grow is minimal. At the end of the process, metal hydroxide gel is formed which is an entangled network of polymeric chains ^[53]. The growth of crystals is arrested. The obtained Ceric hydroxide particles are washed free of anions of ammonia and nitrates and immediately kept in alcohol and thus many alcohol molecules are absorbed by the surface of the particles. Thus the growth and coacervation of Ceric hydroxide nanoparticles is restrained by the protection of alcohol. Calcining the product breaks the gel to form small crystallites. The chances of agglomeration are very less and crystals with very small sizes are obtained.

A small peak is observed at d value of 3.279 in all the samples. The intensity of this peak is highest for sample synthesized with Co-precipitation method. The intensity of this peak is higher for fuel deficient ratio compared to fuel rich ratio for samples synthesized by microwave and combustion methods. The formation of this peak may be due to the fuel lean and fuel rich ratios as they thermodynamically favour formation of certain peaks^[54]. This peak was found to be very close to peak at d value of 3.260 from JCPDS file – no. 441001 for hexagonal structure of Ceria.

3.2 Scanning Electron Microscopy

Scanning electron microscopy (SEM) was done for samples synthesized by combustion (microwave and furnace) method with Stoichiometric ratios, Co-precipitation and Solid State synthesis methods. SEM was done on JEOL make JSM 5610 LV Scanning Electron Microscope. The images were formed by secondary electrons.

The micrograph of sample prepared by solid state synthesis is given in figure C_s 1. The SEM micrograph was taken with accelerating voltage of 5 KV and magnification of 10000. The particles are coarse and highly agglomerated. The particles are in irregular shape with sharp edges and appear to be hard in comparison to samples by furnace and microwave combustion methods. The agglomeration is due to the heat available for long time which causes the crystal to grow larger and agglomerate. The agglomerate size is found to vary from less than 1 μ m to more than 5 μ m as can be seen from the figure. Size distribution is very large. The structure is observed to be pore free.

Scanning electron micrograph of sample prepared by furnace combustion in stoichiometric ratio is given in figure C_s 2. The SEM micrograph was taken with accelerating voltage of 15 KV and magnification of 1000. The microstructure is observed to be fine grained with irregular shaped particles. The agglomeration is very high and the structure is dense. The nature of the product is quite foamy, fluffy and voluminous. Large amount of pores and voids can be seen. The porosity is due to the

large amount of gases escaping during the combustion reaction. The image reveals non-uniform particles and these particles get agglomerated.

For sample prepared by microwave combustion in stoichiometric ratio the micrograph is given in figure C₅ 3. The SEM micrograph was taken with accelerating voltage of 15 KV and magnification of 1000. Here also non uniform grain growth is revealed. The product appears like cotton. The particles are fine and highly agglomerated dense structures. The nature of the product is voluminous and foamy. The primary particles get agglomerated to form larger particles. The porosity observed in the sample is higher compared to sample C₅ 2 as internal heating gives out maximum amount gases. In both the images the surface area of the particle is quite high.

The SEM micrograph of powders prepared by Co-precipitation is given in figure C₅ 4. The SEM micrograph was taken with accelerating voltage of 20 KV and magnification of 3,300. The particles are somewhat round shaped. They are fine and soft in nature. The extent of agglomeration is high with sizes varying from less than 1 μ m to 5 μ m but it is low compared to samples synthesized by furnace and microwave combustion and solid state synthesis. Here also the surface area of the particle is high.

There is a good amount of agglomeration seen in all the structures which may be attributed to the fineness of the particles. Due to high surface to volume ratio the surface effects come into play which may be the cause of the agglomeration.

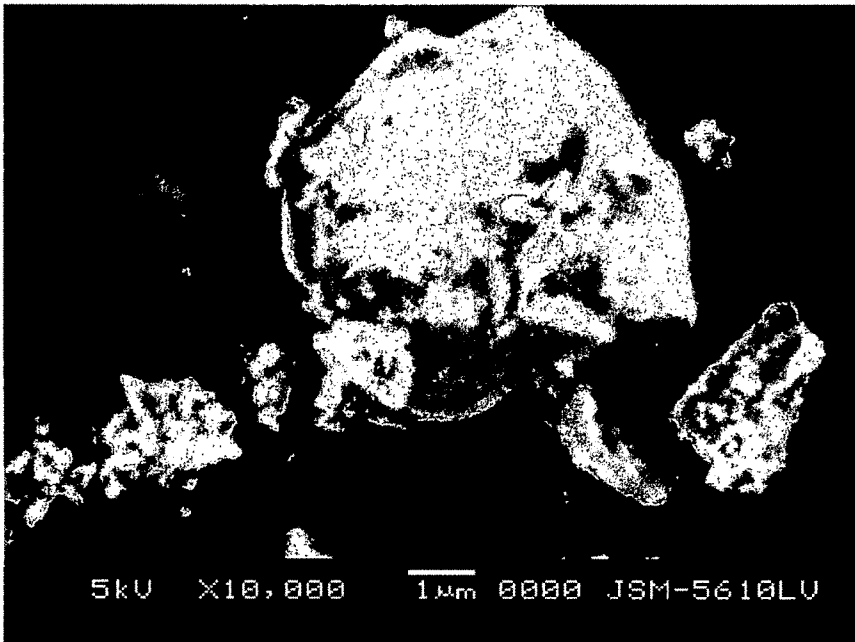


Figure C_s 1 SEM micrographs of CeO₂ synthesized by Solid State Synthesis

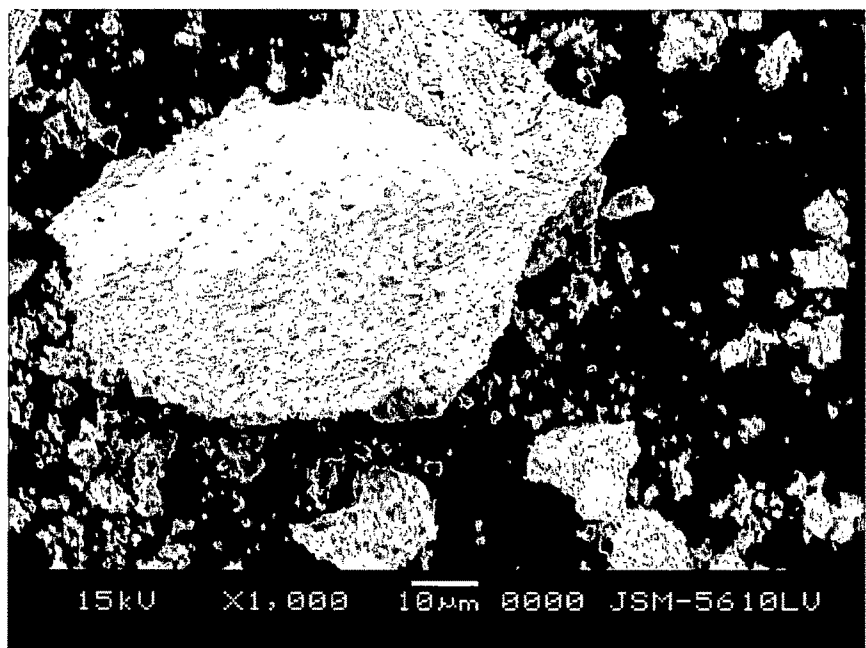


Figure C_s 2 SEM micrographs of stoichiometric CeO₂ synthesized by Furnace combustion synthesis

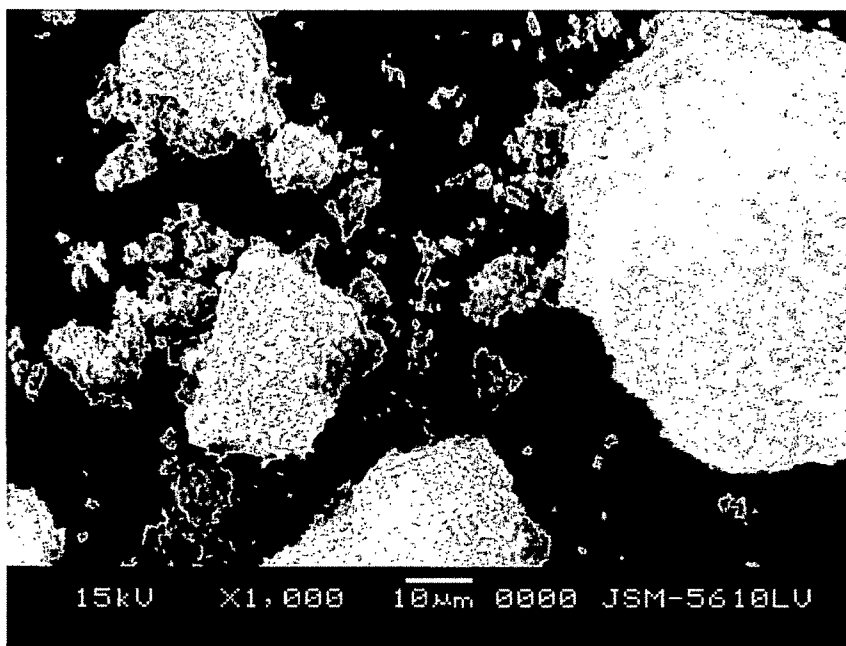


Figure C₅ 3 SEM micrographs of stoichiometric CeO₂ synthesized by Microwave combustion synthesis



Figure C₅ 4 SEM micrographs of CeO₂ synthesized by Co-precipitation

Fluorescence Characteristics

The fluorescence characteristics of the samples were recorded on a *Fluoromax 4* instrument of *Horiba Jobin Yvon* make, USA. Equal amount of samples were taken in each case. The slit width for the excitation as well as emission monochromators was fixed at 1 nm to ensure optimization and uniformity. The integration time was kept at 0.1 second.

To begin with, a random check was carried out for the emission lines. These emission lines were then used to get the exact excitation features. The reported emission spectra were taken for these precise excitation wavelengths. Thereafter, the excitation spectra were recorded for the obtained emission lines. The results are as under.

CeO₂: Eu⁺³

Figure CEF1b shows emission spectra of sample C2 synthesized by solid state synthesis. The emission characteristics were recorded for three different excitation wavelengths 367, 466 and 526 nm. Four distinct emission peaks are observed at 590, 609, 631 and 654 nm respectively. The intensities of all the emission peaks are highest for excitation wavelength 367 nm, followed by emission intensities at excitation wavelengths 466 and 526 nm respectively. It is observed that the intensity of the emission peak at 590 nm is highest followed by peaks at 631 nm and 609 nm at the excitation wavelength 367 nm. For excitation wavelength 466 nm, the 590 nm peak has the relatively lower intensity and the other peaks at 609 and 631 nm have relatively higher intensities in the same order. The intensity pattern for 526 nm excitation has the same trend as observed for 367 nm.

Figure CEF1a shows excitation spectra of sample C2. The excitation spectrum was recorded by monitoring the four emission wavelengths mentioned above i.e. 590, 609, 631 and 654 nm. One broad band is observed at 367 nm and other narrow peaks at 466, 526, 532, 538 and 547 nm. The intensity of 466 nm peak is significantly higher than the other narrow peaks. For emission wavelength 590 nm, the excitation intensity of the broad band is highest. The overall excitation intensity for rest of the peaks is highest

for emission wavelength 631 nm followed by 609, 590, 654 nm respectively. It is observed that the intensity of the excitation broad band varies abruptly for the different monitoring lines. The emission peak of 590 nm can be largely ascribed to the broad excitation peak of 367 nm while the other emission peaks derive energy predominantly from the narrow band excitations at 466, 526, 532 and 538 nm.

Figure CEF2b shows emission spectra of sample C3 synthesized by Furnace combustion synthesis with fuel rich ratio. The emission characteristics were recorded for three different excitation wavelengths 352, 466 and 526 nm. Four distinct emission peaks are observed at 590, 609, 631 and 654 nm respectively. The intensity the main emission peak at 590 nm is the highest for excitation wavelength 352 nm. For the excitation wavelengths 466 and 526 nm, the emission peak intensities are quite low.

Figure CEF2a shows excitation spectra of sample C3. The excitation spectrum was recorded by monitoring the four different emission wavelengths i.e. 590, 609, 631 and 654 nm. There is one broad band at 352 nm, two narrow peaks at 466 & 526 nm and other minor peaks at 532, 538 and 547 nm. The intensity of the broad band is highest for emission wavelength at 590 nm. The excitation intensities for the other emission lines are significantly subdued. Unlike sample C2, the 526 nm excitation peak has a higher intensity compared to excitation 466 nm. It is to be noted that the broad band has shifted to 352 nm in this case.

Figure CEF3b shows emission spectra of sample C4 synthesized by Furnace combustion synthesis with stoichiometric ratio. The emission characteristics were recorded for three different excitation wavelengths 352, 466 and 526 nm. There are four distinct emission peaks observed at 590, 609, 631 and 654 nm respectively. The intensity of the emission peak at 590 nm is highest for excitation wavelength at 352 nm. The intensity of the emission peaks at 609 and 631 nm are relatively high. However, the distribution of intensities over the three emission peaks for different excitation wavelengths does not follow the same trend.

Figure CEF3a shows excitation spectra of sample C4. The excitation spectrum was recorded by monitoring the four different emission wavelengths i.e. 590, 609, 631 and

654 nm. The broad band at 352 nm remains as in the case of the previous sample as do the other peaks. The intensity of the broad band is highest for emission wavelength at 590 nm followed by 631, 609 and 654 nm respectively. In general, the same trend remains as in other samples.

Figure CEF4b shows emission spectra of sample C5 synthesized by Furnace combustion synthesis with fuel lean ratio. The emission characteristics were recorded for three different excitation wavelengths 352, 466 and 526 nm. There are four emission peaks observed at 590, 609, 631 and 654 nm respectively. The intensity of the 590 nm emission peak is the highest for excitation wavelength at 352 nm. The other emission peaks are almost relegated to the background.

Figure CEF4a shows excitation spectra of sample C5. The excitation spectrum was recorded by monitoring the four different emission wavelengths i.e. 590, 609, 631 and 654 nm. The same features are repeated in this sample too. The broad band is at 352 nm with very high intensity for the 590 nm emission line. For the other emission lines, the excitation intensities are found to be too low.

Figure CEF5b shows emission spectra of sample C6 synthesized by Microwave combustion synthesis with fuel rich ratio. The emission characteristics were recorded for three different excitation wavelengths 353, 466 and 526 nm. There are four emission peaks observed at 590, 609, 631 and 654 nm. The intensity of the emission peak at 590 nm decreases for excitation wavelengths 353, 526 and 466 nm in the same order. The emission peaks at 609 and 631 nm are broadened in this case, although their intensities are low. The 654 nm peak is almost like a hump.

Figure CEF5a shows excitation spectra of sample C6. The excitation spectrum was recorded by monitoring the three different emission wavelengths i.e. 590, 609, 631 nm. There is one broad band at 353 nm and other peaks observed at 466, 526, 532, 538 and 547 nm. The intensity of the broad band is highest for emission wavelength at 590 nm followed by 609 and 631 nm respectively. The relative intensities of the excitation peaks at 466 nm and 526 nm is quite high.

Figure CEF6b shows emission spectra of sample C7 synthesized by Microwave combustion synthesis with stoichiometric ratio. The emission characteristics were recorded for three different excitation wavelengths 352, 466 and 526 nm. There are four emission peaks observed at 590, 609, 631 and 654 nm respectively. The intensities of all the emission peaks are highest for excitation wavelength 352 nm followed by 526 nm. The emission features for excitation wavelength 466 nm shows a different trend. The 590-nm emission peak is sharp and intense. The intensities of the other peaks is relatively low.

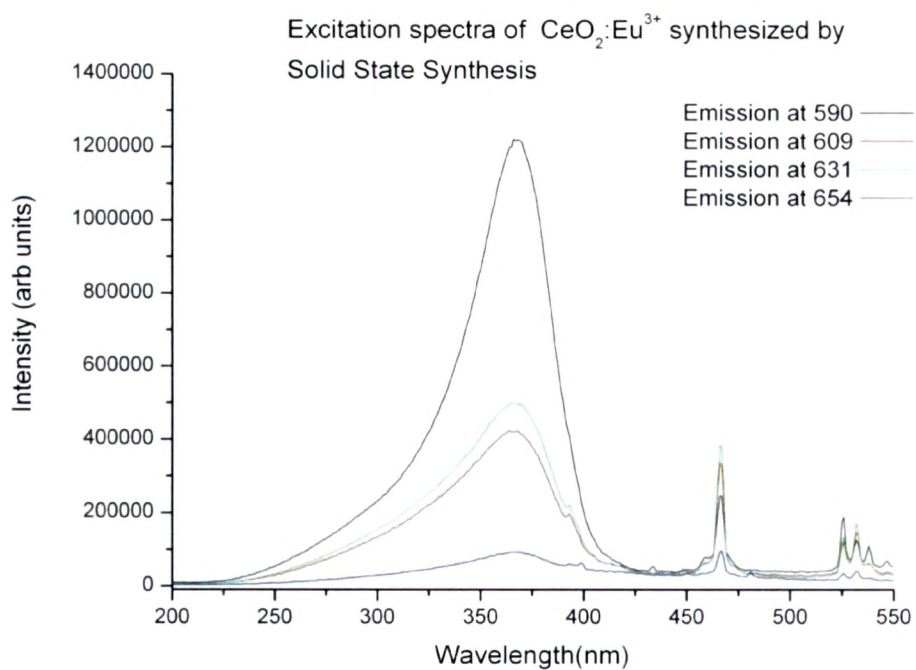
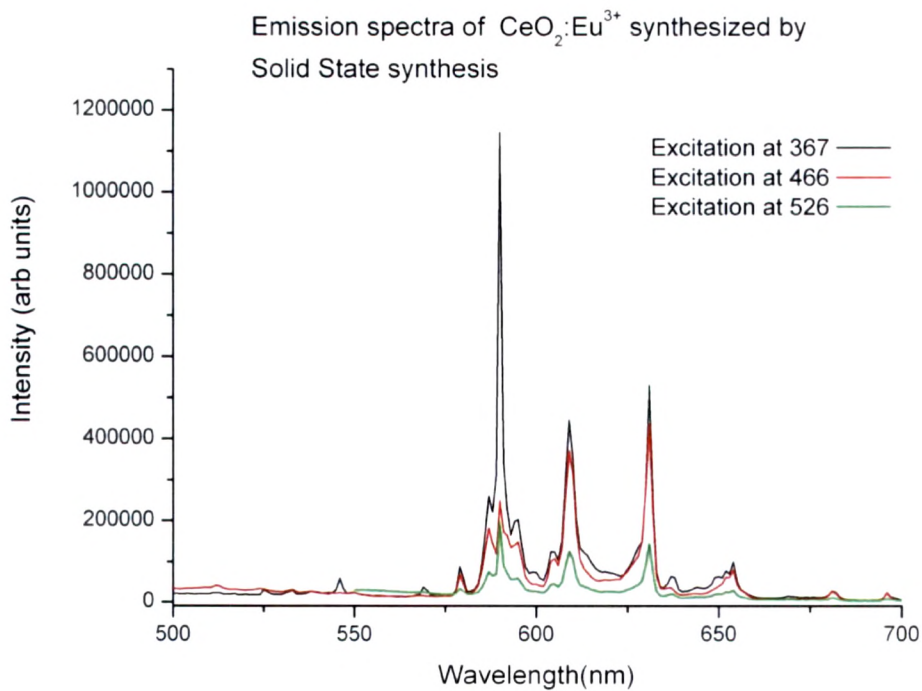
Figure CEF6a shows excitation spectra of sample C7. The excitation spectrum was recorded by monitoring the four different emission wavelengths i.e. 590, 609, 631 and 654 nm. There is one broad band at 352 nm and other peaks at 466, 526, 532, 538 and 547 nm. The other features are exactly identical i.e. the intensity of the broad band feature for the 590 nm emission line is the highest. Intensities of the other features are comparatively too low.

Figure CEF7b shows emission spectra of sample C8 synthesized by Microwave combustion synthesis with fuel lean ratio. The emission characteristics were recorded for three different excitation wavelengths 357, 466 and 526 nm. Four emission peaks are observed at 590, 609, 631 and 654 nm respectively. A striking feature of the characteristics is the broadening of all the three major peaks. Splitting of peaks is also observed. The relative intensities are also high.

Figure CEF7a shows excitation spectra of sample C8. The excitation spectrum was recorded by monitoring the four different emission wavelengths i.e. 590, 609, 631 and 654 nm. There is one broad band at 357 nm and other peaks at 466, 526, 532, 538 and 547 nm. The excitation spectra is different from other samples in the sense that the intensities of the broad band as well as the two major narrow band peaks are of the same order. There are several new features although insignificant in terms of intensity.

Figure CEF8b shows emission spectra of sample C9 synthesized by Co – precipitation method. The emission characteristics were recorded for three different excitation wavelengths 345, 465 and 526 nm. There are four emission peaks observed at 590, 604, 628 and 650 nm. The intensity of the 590 nm peak relative to the other peaks is the highest among all samples. The dominant feature is absolutely sharp and intense while the others are practically redundant.

Figure CEF8a shows excitation spectra of sample C9. The excitation spectrum was recorded by monitoring the three different emission wavelengths i.e. 590, 604, 628. There is one broad band at 345 nm and five other peaks observed at 465, 526, 532, 538 and 547 nm. There is a visible shift in the peak wavelength of the broad band feature towards the lower side i. e. 345 nm. The relative intensity of the 526 nm excitation peak for the monitoring line 590 nm is unusually high.

**Figure: CEF1a****Figure: CEF1b**

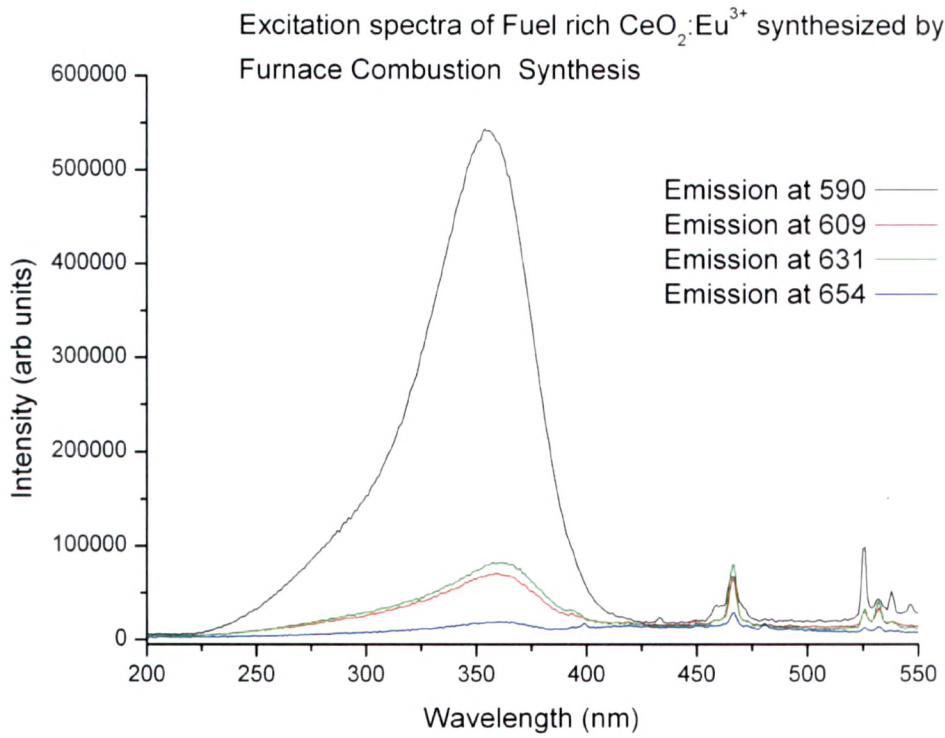


Figure: CEF2a

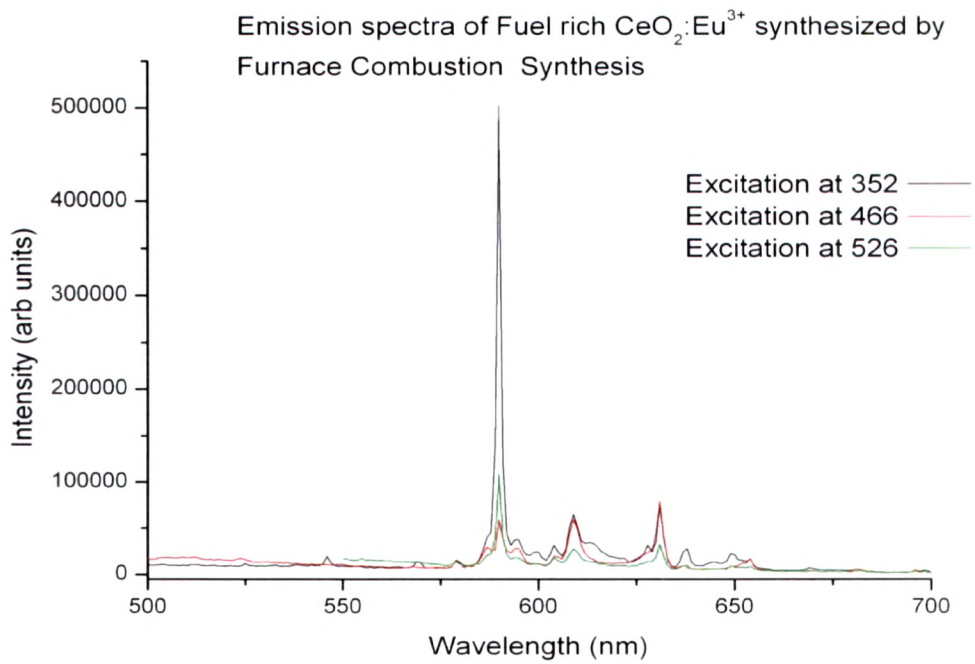
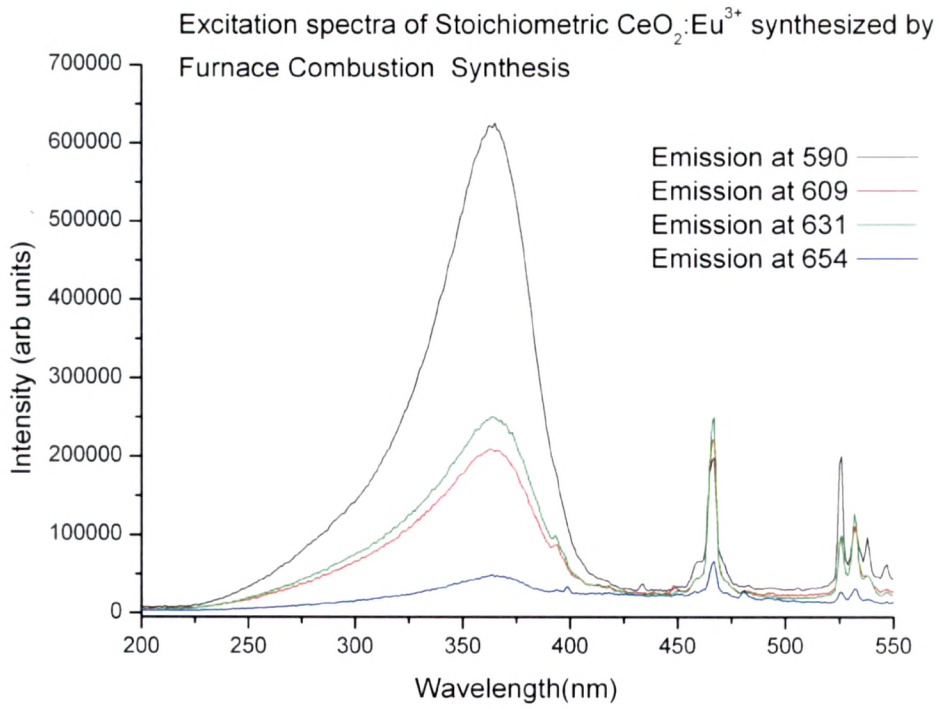
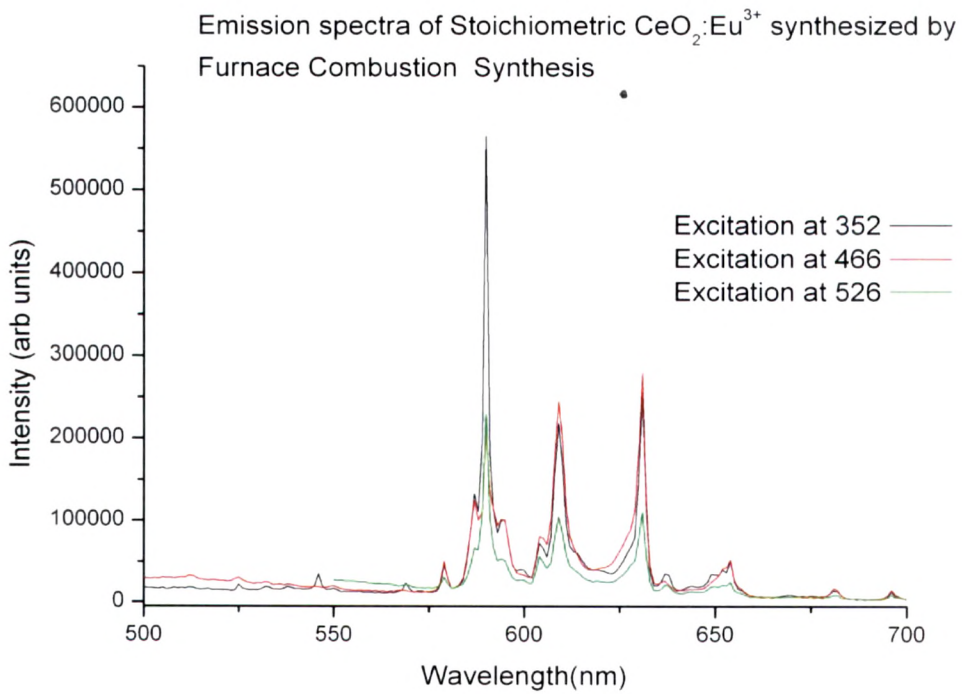


Figure: CEF2b

**Figure: CEF3a****Figure: CEF3b**

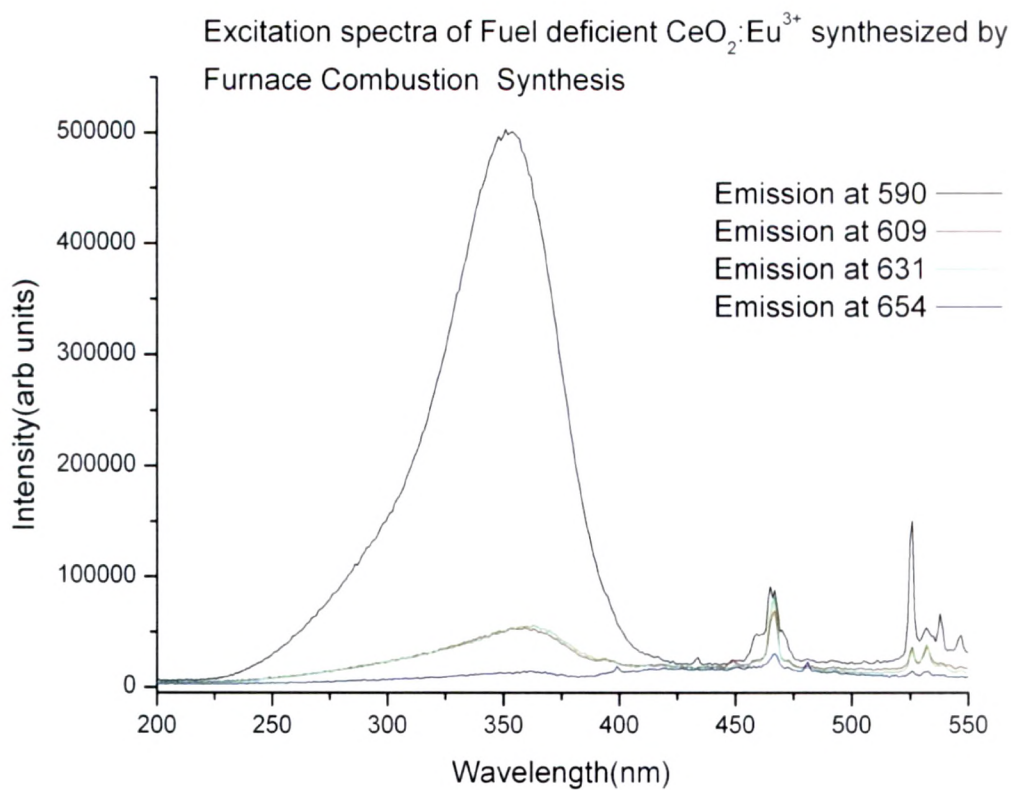


Figure: CEF4a

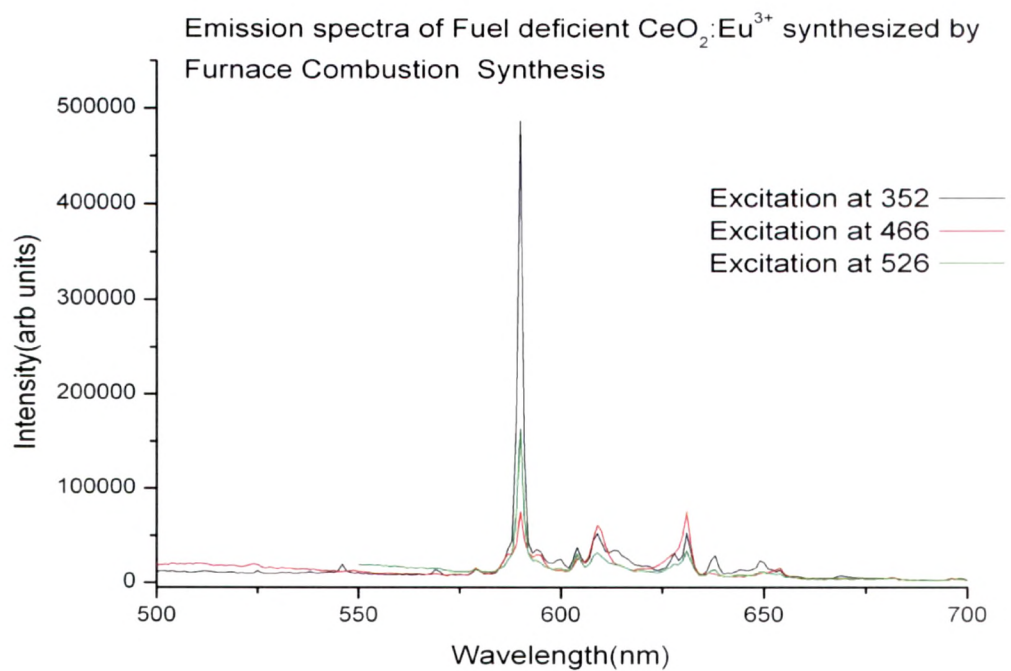
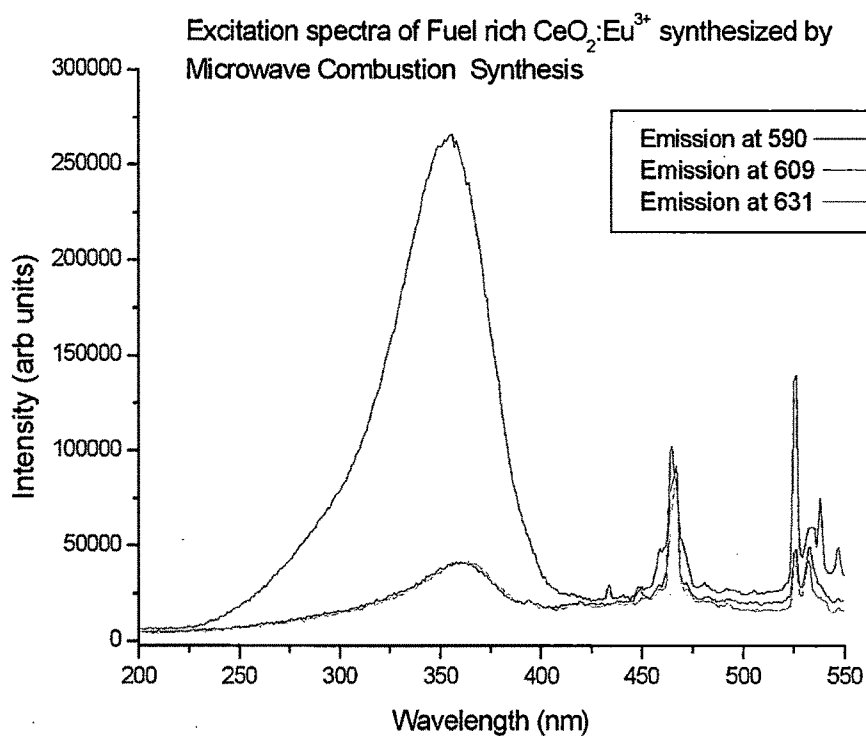
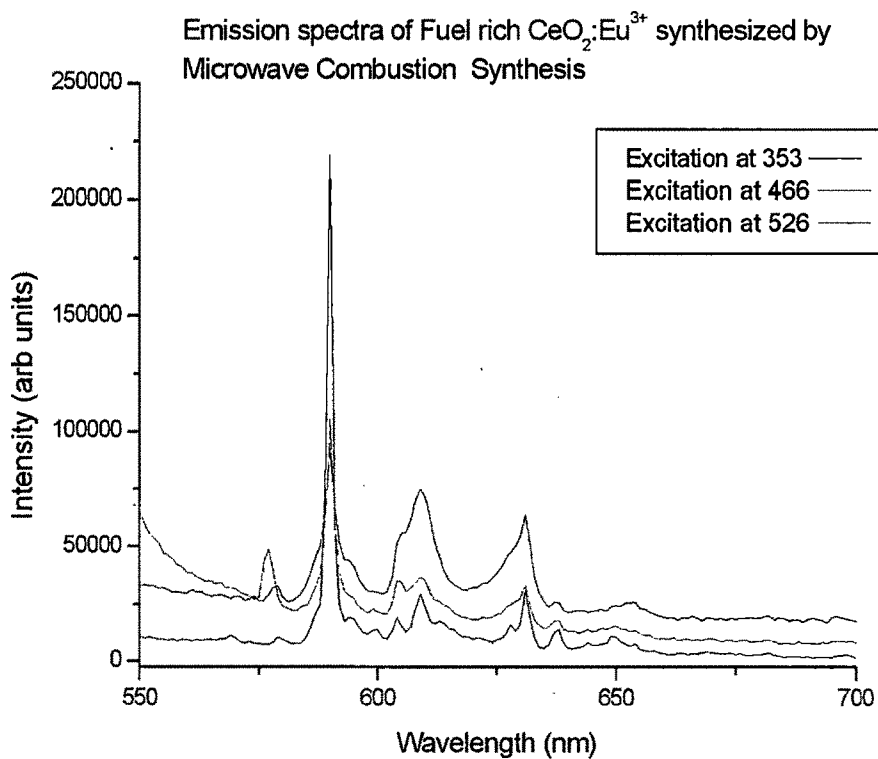


Figure: CEF4b

**Figure: CEF5a****Figure: CEF5b**

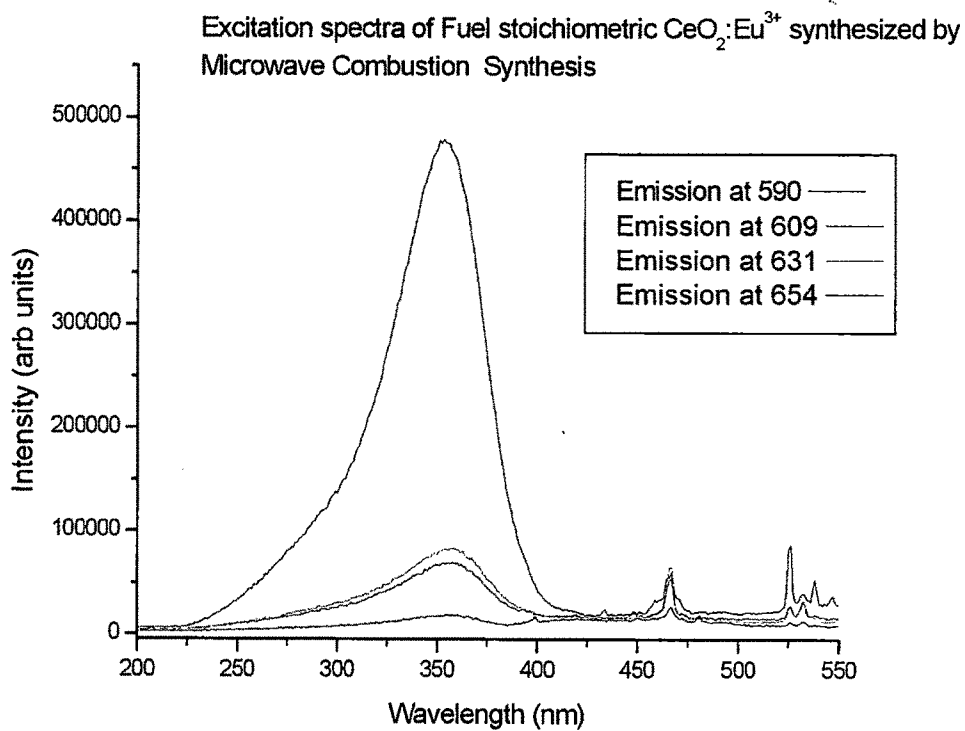


Figure: CEF6a

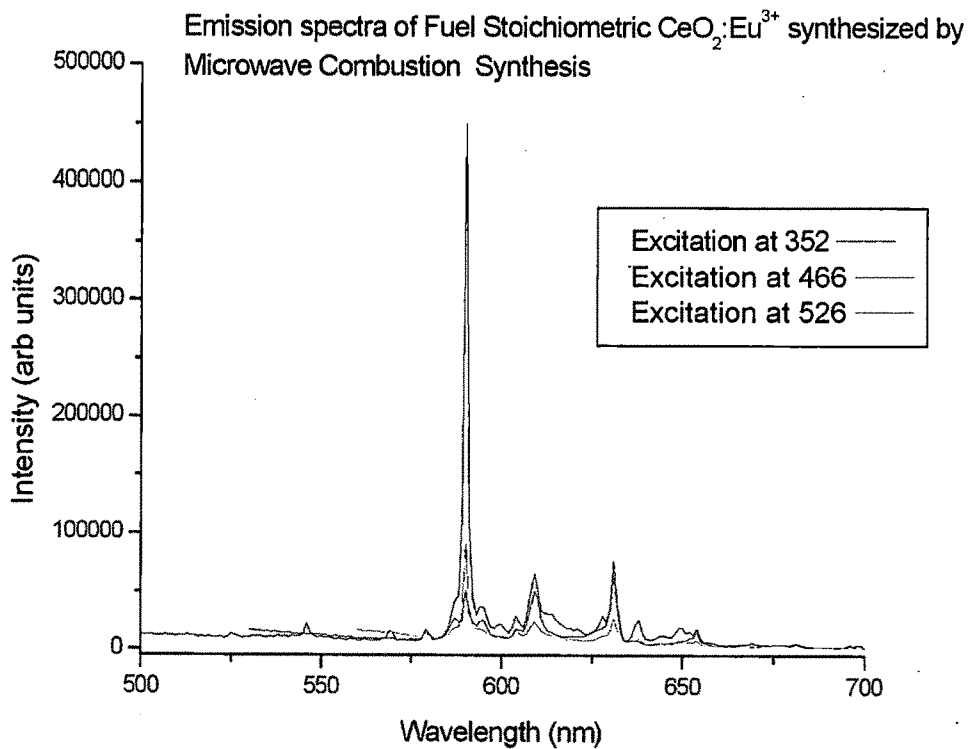
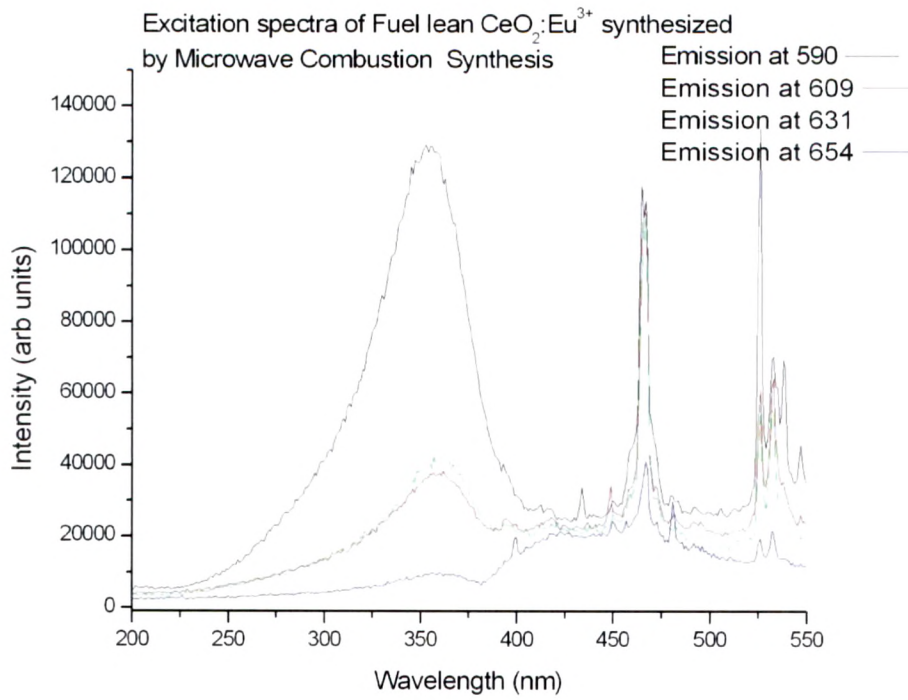
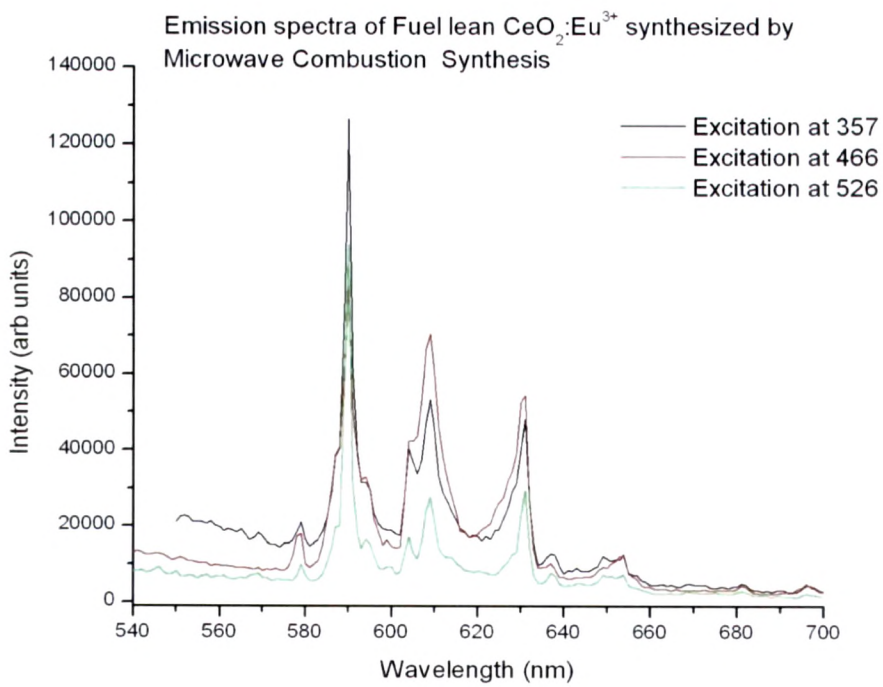


Figure: CEF6b

**Figure: CEF7a****Figure: CEF7b**

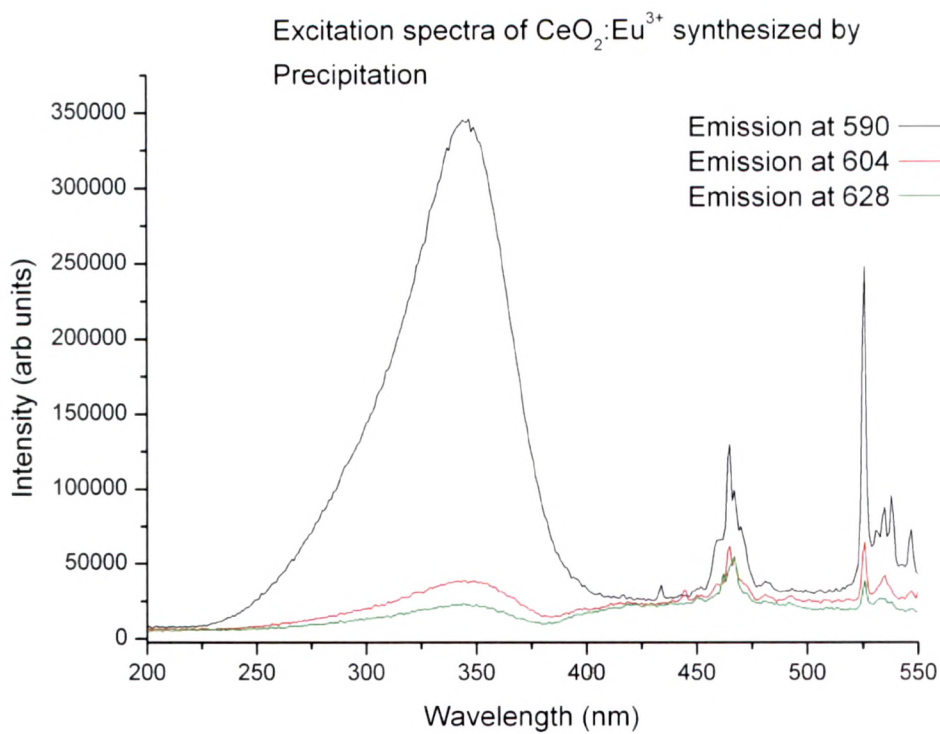


Figure: CEF8a

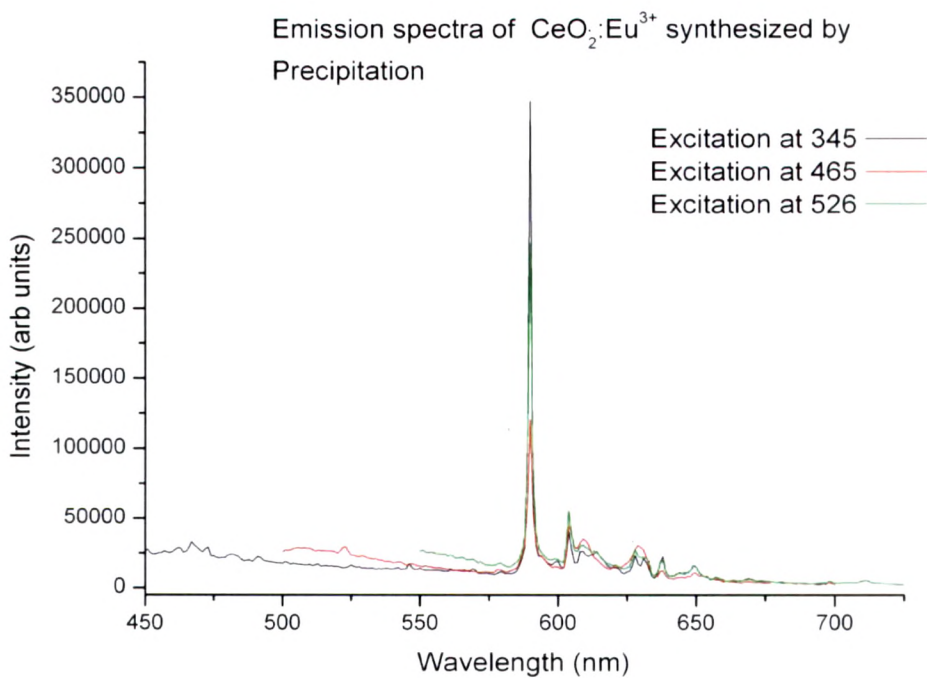
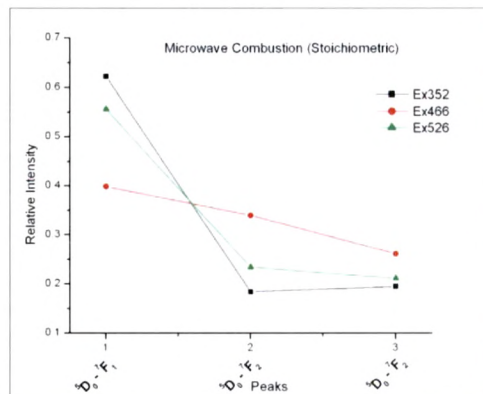
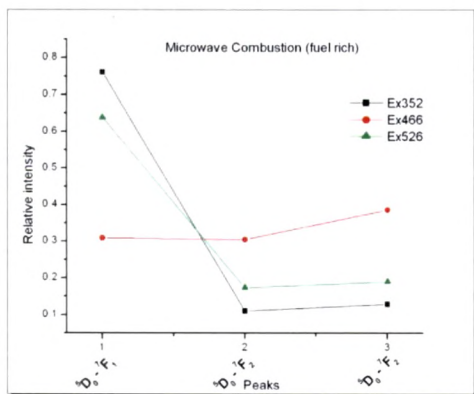
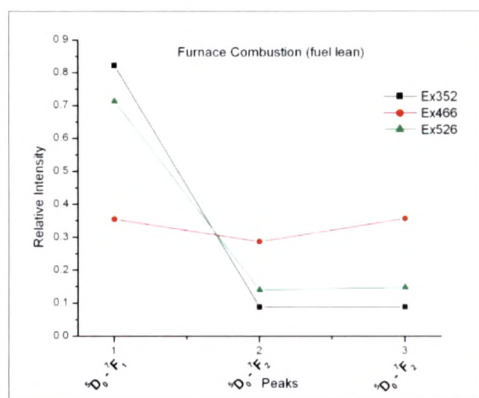
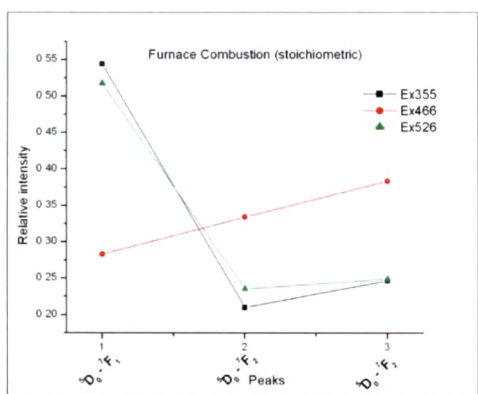
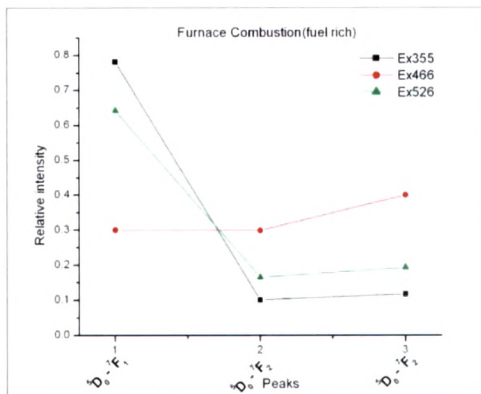
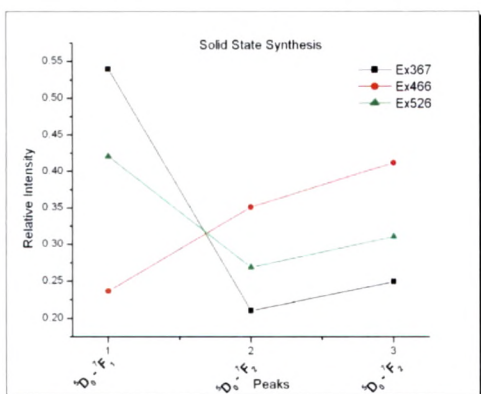
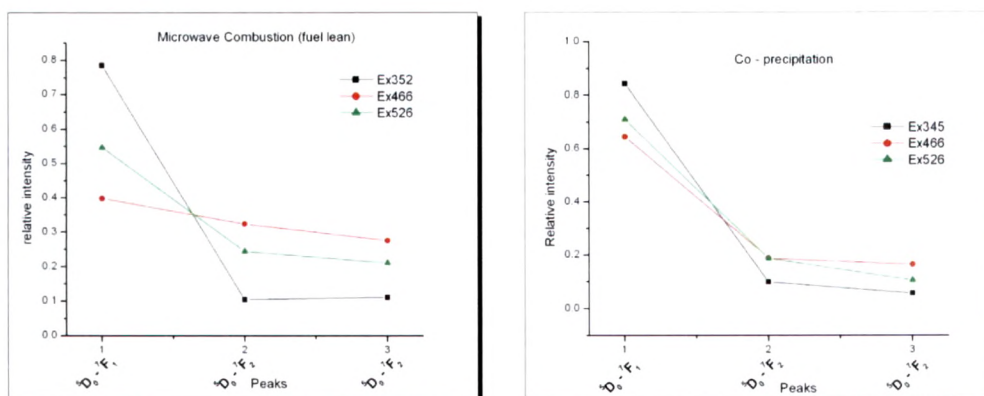


Figure: CEF8b

The activation of Ceria by Europium has been reported earlier ^[12, 39]. However, this study attempts to investigate the optical properties of Europium doped Ceria synthesized by easy and time saving methods of combustion. For the purpose of reference, one sample has been prepared by the usual method of solid state synthesis. While the later method gives bulk material, the former ones yield nano crystalline material. For the sake of comparison, one sample was made by co-precipitation method to get nano particles. Thus a range of materials from bulk to nanocrystal to nanoparticles have been synthesized. This is borne out by the XRD results. It has been interesting to see the results of fluorescence spectra in the light of these results.

The results of the fluorescence spectra confirm the incorporation of Europium in the Ceria lattice in the +3 state. The transitions of Eu^{3+} are given by ${}^5\text{D}_0 \rightarrow {}^7\text{F}_J$ ($J = 0, 1, 2, 3, 4$) are authentically pronounced in these spectra ^[55]. The relative intensities of these transitions vary from sample to sample. The major emission peak in all the samples has been found to be at 590 nm, ascribed to the ${}^5\text{D}_0 \rightarrow {}^7\text{F}_1$ transition, which operates by magnetic dipole interaction ^[56]. This transition is not affected by the crystal field. The other peaks at 609 nm, 632 nm (${}^5\text{D}_0 \rightarrow {}^7\text{F}_2$) and 654 nm (${}^5\text{D}_0 \rightarrow {}^7\text{F}_3$) are electric dipole transitions ^[57, 58]. These transitions are affected by the crystal field. The distribution of energy among the three major peaks (590 nm, 609 nm and 632 nm) is graphically represented in the figures below for the respective samples. The figures give intensity distribution of the emission for three different excitation wavelengths 366 nm, 466 nm and 526 nm.

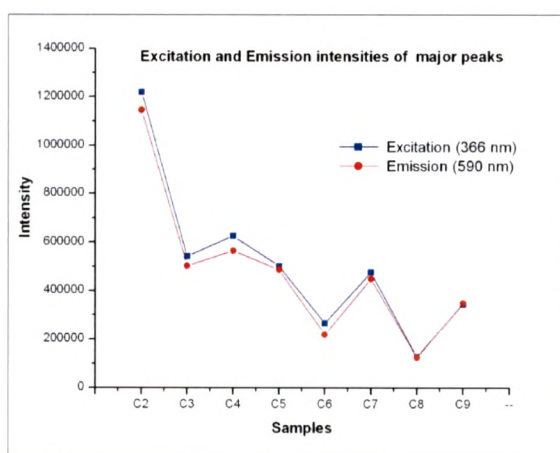




It can be seen from the above figures that the intensity distribution over the peaks for the excitation wavelengths 366 nm and 526 nm follow similar trends for all samples. However, for the 466 nm excitation, a lot of variation is observed in the distribution of intensities. This indicates that the energy transfer from the 466 nm excitation peak to the emission levels is sensitive to the surrounding environment. The only exception to the above trend is the sample prepared by co-precipitation method, where intensity distribution over the emission peaks follows the same pattern for every excitation wavelength. Since the sample in question is constituted of nano particles of small size, it leads to a speculation that reduction in particle size has led to stabilization of the 466 nm excitation level also. However, its confirmation would need further studies.

The analysis of the emission spectra of the samples reveals that the emission features are the most intense for the sample made by solid state synthesis. For the sample prepared by co-precipitation method, which has the smallest particle size, the 590 nm peak is the most dominant while others are redundant. The effect of reduction in particle size is known to alter the energy levels and hence the transition probabilities. The dominance of the 590 nm peak in this case can be attributed to the reduction in the particle size. For the samples prepared by combustion synthesis, the stoichiometric composition by furnace combustion has emission characteristics nearest to the bulk sample. The samples prepared by microwave assistance show broadening and splitting for fuel lean and fuel rich samples. For the rest of the samples, the intensity of the dominant 590 nm peak is relatively very high.

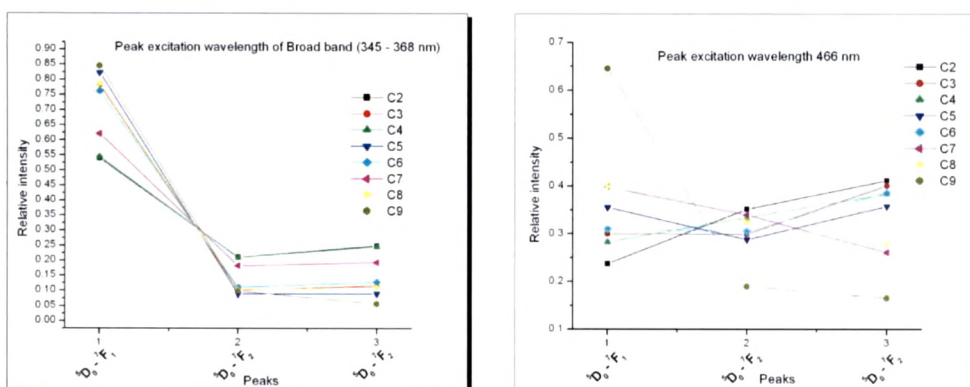
The variation of intensities of the major excitation (366 nm broad band) and emission (590 nm) peaks for the prepared samples are presented graphically in the figure below. It shows some distinct features. The absorption and emission is maximum for the sample C2 prepared by solid state method. This is followed by the samples prepared by furnace combustion method (average for C3, C4 and C5) and microwave combustion method (average for C6, C7 and C8). Although the intensities are on the lower side for the sample C9, the striking feature is that the excitation and emission intensities are the same, suggesting almost cent percent energy conversion of the absorbed energy into the emission lines. It needs to be noted here that the intensities of excitation and emission peaks other than those mentioned above have not been considered. The sample in question consists of nanoparticles. With further reduction in particle size and surface passivation, the quantum of the absorbed energy can be significantly enhanced.



The analysis of the excitation spectra assumes increased significance. As discussed above, the bulk sample prepared by solid state synthesis at one end has the highest crystallite size while the nano particles synthesized by co-precipitation method have the lowest particle size at the other end of the scale. A co-relation can be established between the particle size and the peak excitation wavelength of the dominant broad band excitation feature ^[12]. While the peak excitation wavelength has been recorded to be 368 nm for the bulk sample, a substantial blue shift has been observed in the case of later. The peak was found to be at 345 nm. The change in the peak excitation wavelength of the samples made by combustion synthesis methods also corroborates

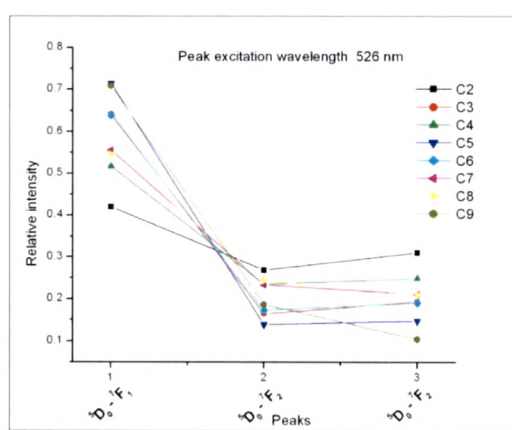
this. The peak excitation wavelength of the samples with stoichiometric proportions, which have bigger particle size (16 nm for furnace made) have been observed to be on the higher side (365 nm) compared to those with fuel rich proportions, which have comparatively smaller particle size (12 nm for furnace made) and consequently lower peak excitation wavelengths (355 nm).

The distribution of energy to the respective transitions by each of the major excitation peaks in all the prepared samples is presented below. It is evident that the energy distribution by the broad excitation peak, which varies between 345 nm to 368 nm, and by the excitation peak 526 nm follow similar patterns. The energy distribution from the 466 nm excitation peak varies from sample to sample. However, the sample prepared by co-precipitation method follows the same pattern of energy distribution for all the excitation wavelengths.

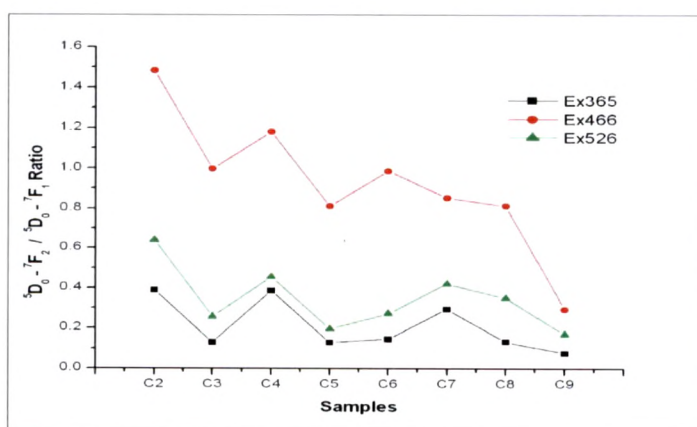


The dominant excitation peak, which is a broad band feature can be attributed to the energy absorption by the host lattice i.e. CeO_2 [12, 55]. The multiplicity of the excitation energy levels in the host lattice leads to absorption at multiple levels, giving a broad band feature. The narrow band excitation features can be attributed to the Eu^{3+} ions. The energy absorbed by the charge transfer from O^{2-} valence band to Ce^{4+} conduction band is transferred to the Eu^{3+} and it produces red emission. The intra $4f^n$ transitions are also responsible for the excitation-emission mechanism. The $\text{Eu}-\text{O}$ bond also plays important role in the energy transfer mechanism [59]. The interactions are in terms of magnetic and electric dipole transitions [39].

The 590 nm peak (${}^5D_0 \rightarrow {}^7F_1$ magnetic dipole transition) dominates the emission spectra, when the Eu^{3+} ions are located at sites with inversion symmetry. If the Eu^{3+} ions are located at sites without inversion symmetry, the 609 nm peak (${}^5D_0 \rightarrow {}^7F_2$ electric dipole transition) dominates [55]. Hence, increase in the 609 nm peak intensity is indicative of the increasing distortion of the local field around Eu^{3+} ions. The ratio of intensity of these two peaks i.e. (${}^5D_0 \rightarrow {}^7F_2 / {}^5D_0 \rightarrow {}^7F_1$) quantifies the degree of distortion from the inversion symmetry of the local environment of Eu^{3+} ions in the host lattice. Hence, lower the ratio, better is the inversion symmetry of Eu^{3+} ions.



The figure given below shows this variation of degree of distortion for the prepared samples for the different excitation wavelengths. As expected, the ratio is minimum for the 365 nm excitation broad band, the major source of energy for the 590 nm emission peak (${}^5D_0 \rightarrow {}^7F_1$) and maximum for the 466 nm excitation line, which has been observed to be site sensitive.



CeO₂: Tb⁺³

The samples of Terbium doped Ceria were prepared by the same methods as mentioned above. Total eight samples were prepared. The concentration of Terbium was kept constant at 2 molar percent for all samples. The fluorescence characteristics of the samples were recorded on a **Fluoromax 4** instrument of **Horiba Jobin Yvon** make, USA. Equal amount of samples were taken in each case. The slit width for the excitation as well as emission monochromators was fixed at 1 nm to ensure optimization and uniformity. The integration time was kept at 0.1 second.

To begin with, a random check was carried out for the emission lines. These emission lines were then used to get the exact excitation features. The reported emission spectra were taken for these precise excitation wavelengths. Thereafter, the excitation spectra were recorded for the obtained emission lines. The results are given below. The excitation and emission characteristics are similar for all the samples, although they are not as pronounced as the ones with Europium activation. The emission line is found to be specifically around 544 nm, which is the characteristic emission line of Terbium in the +3 valence state. This emission line is attributed to the $^5D_4 \rightarrow ^7F_5$ transition of the Tb³⁺ ion^[60]. This transition is insensitive to the crystal field splitting on account of the strong shielding by the orbital electrons.

The excitation spectrum has two peaks at 400 nm and 497 nm. The 497 nm peak has a higher intensity compared to the 400 nm peak for all the samples. Since both peaks are narrow band features, they can be attributed to the Tb³⁺ states. In this case, there is no major absorption either in the narrow band domain or in the broad band domain. The broad band is either due to the host lattice or charge transfer states, which is nonexistent here. Hence there is no significant excitation. It would be interesting to note that Cerium and Terbium act as excellent sensitizer and activator in several host lattices. While the valence state of Cerium in such cases is always +3, in this case it is +4. That is another reason for the poor excitation and the subsequent emission characteristics.

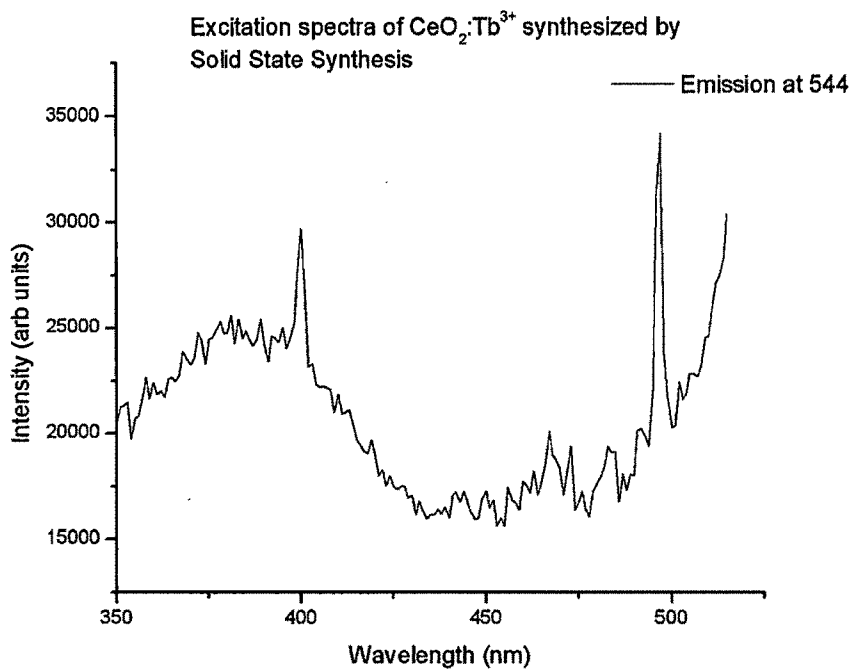


Figure: CTF1a

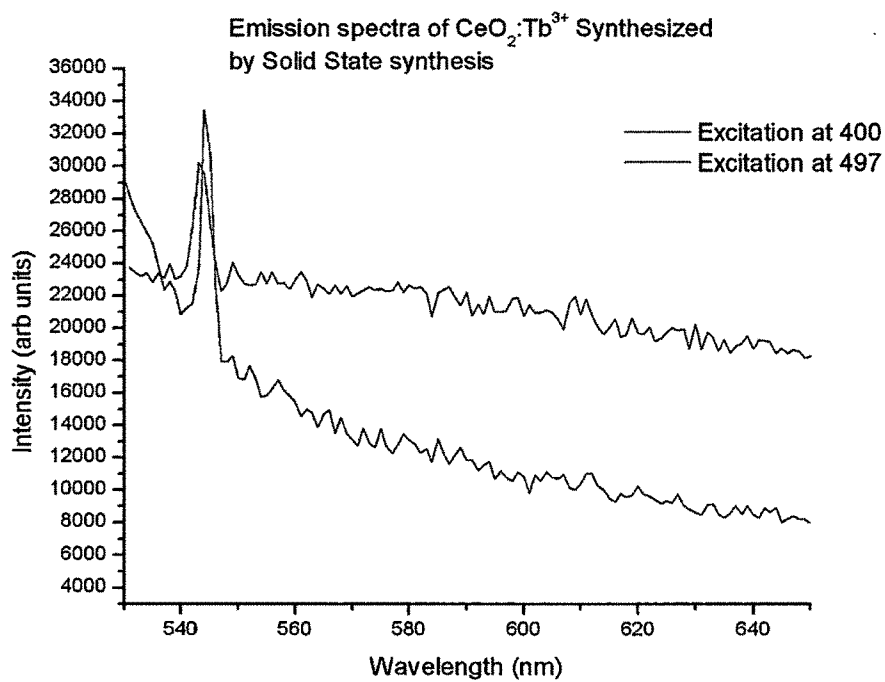


Figure: CTF1b

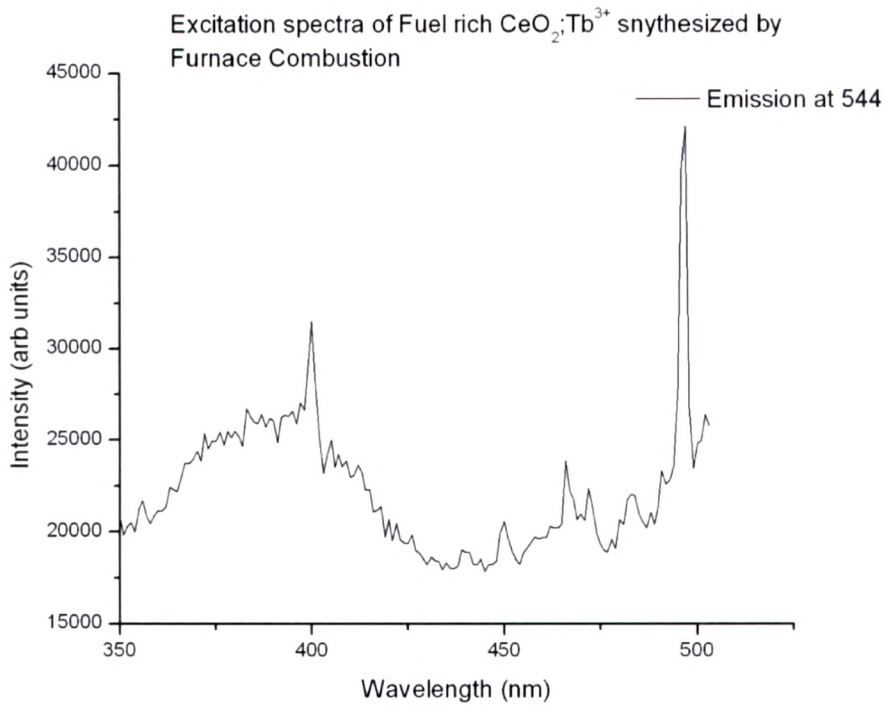


Figure: CTF2a

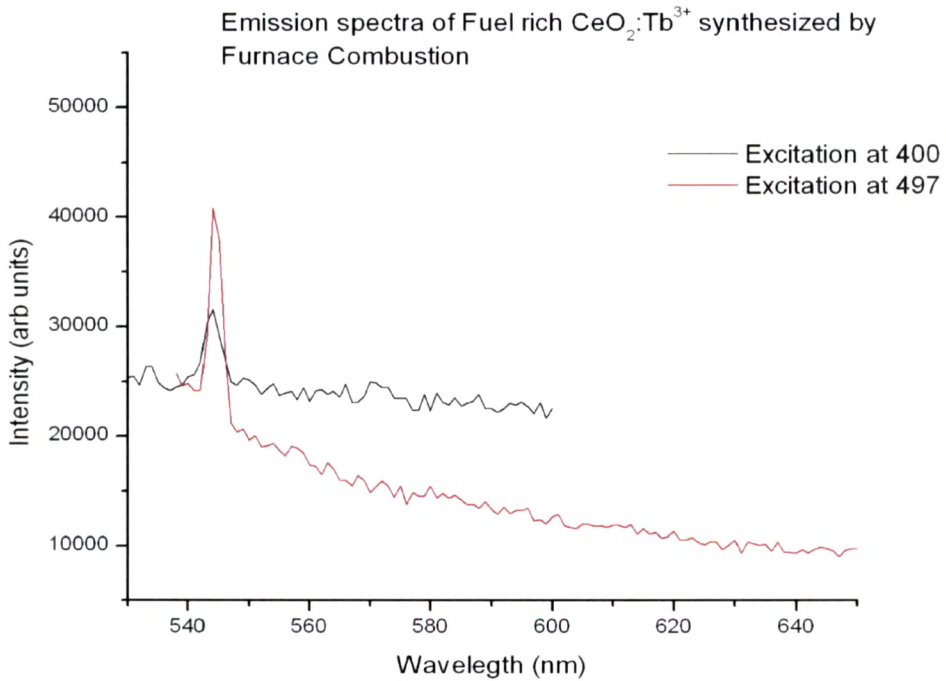


Figure: CTF2b

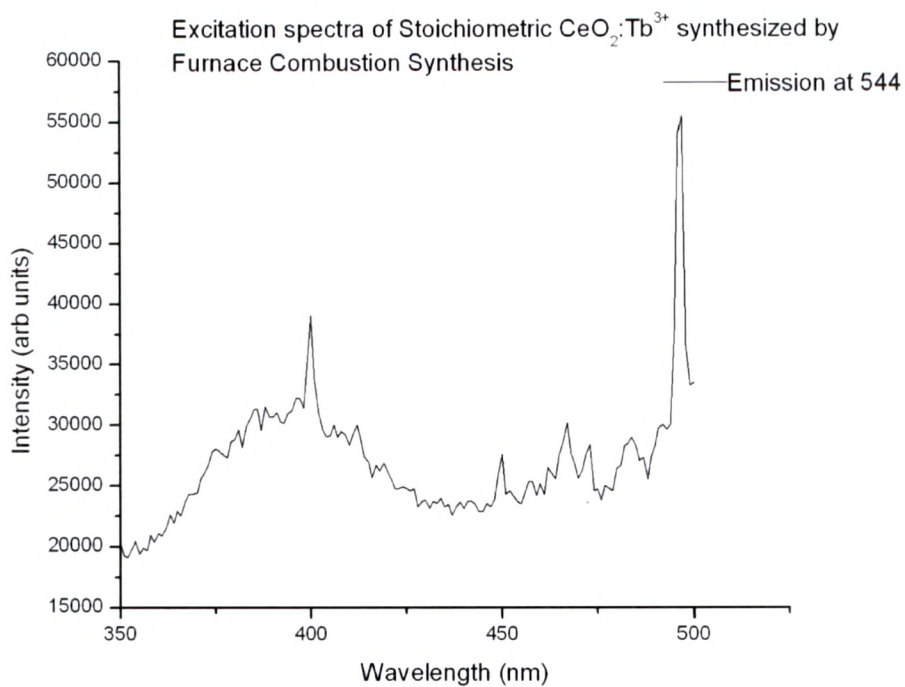


Figure: CTF3a

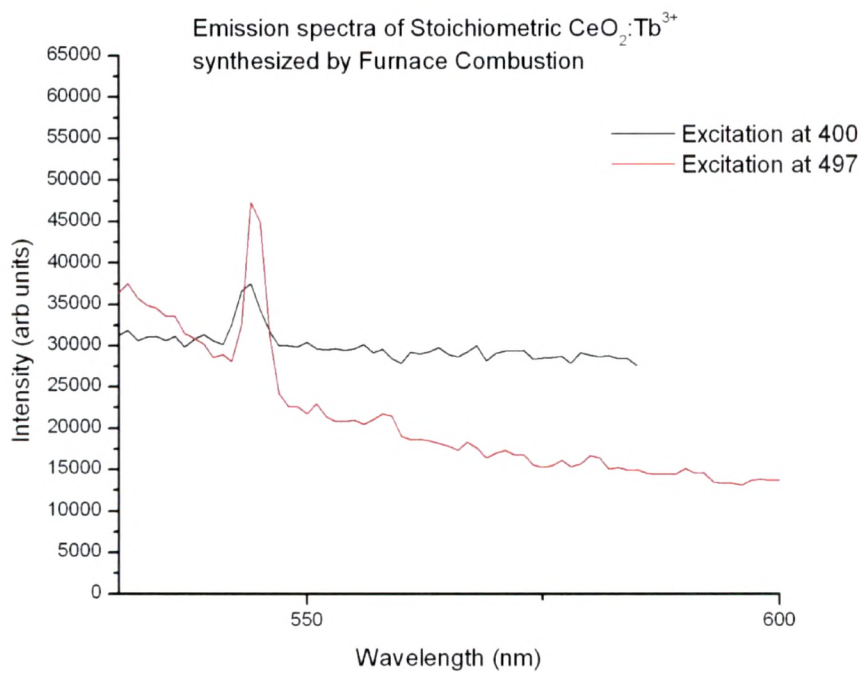
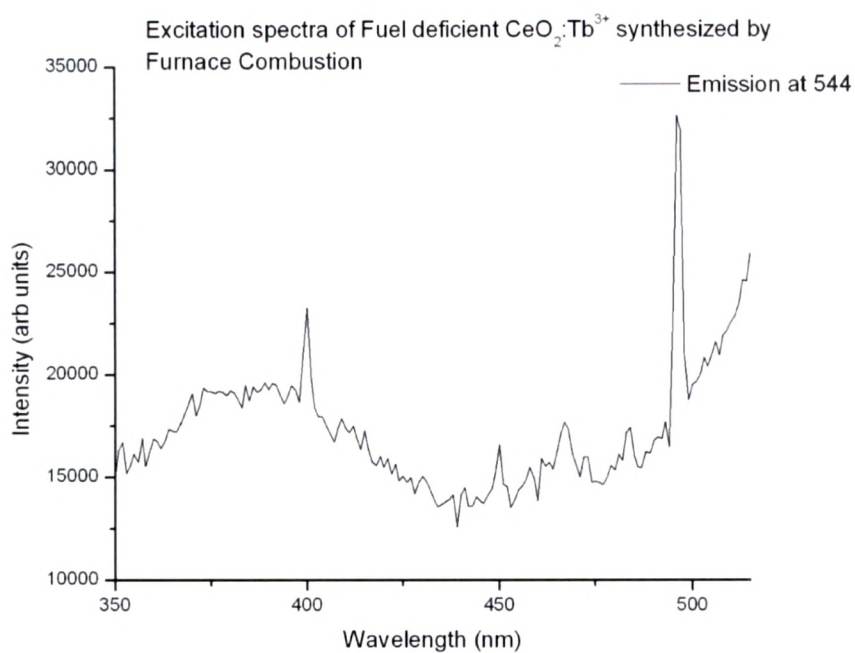
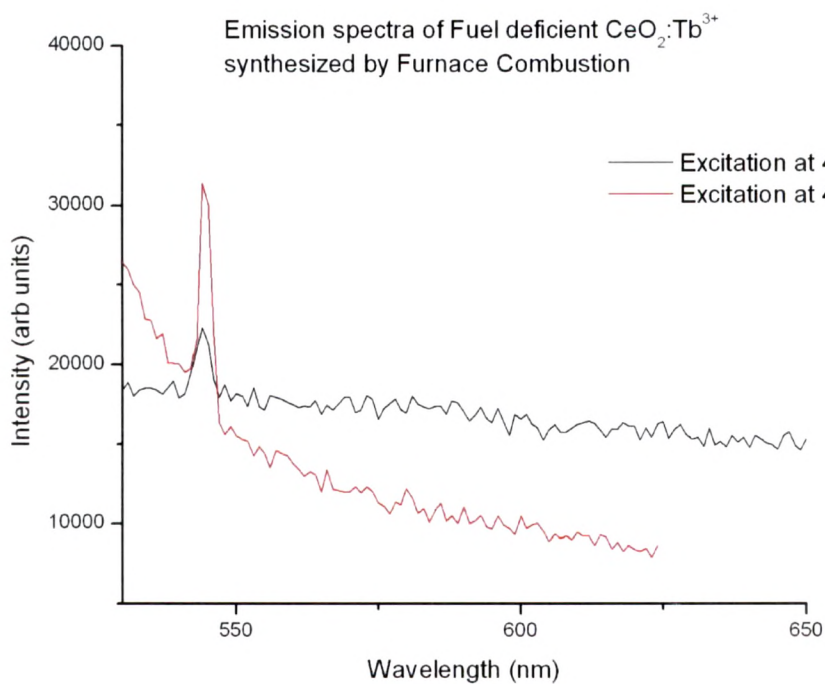
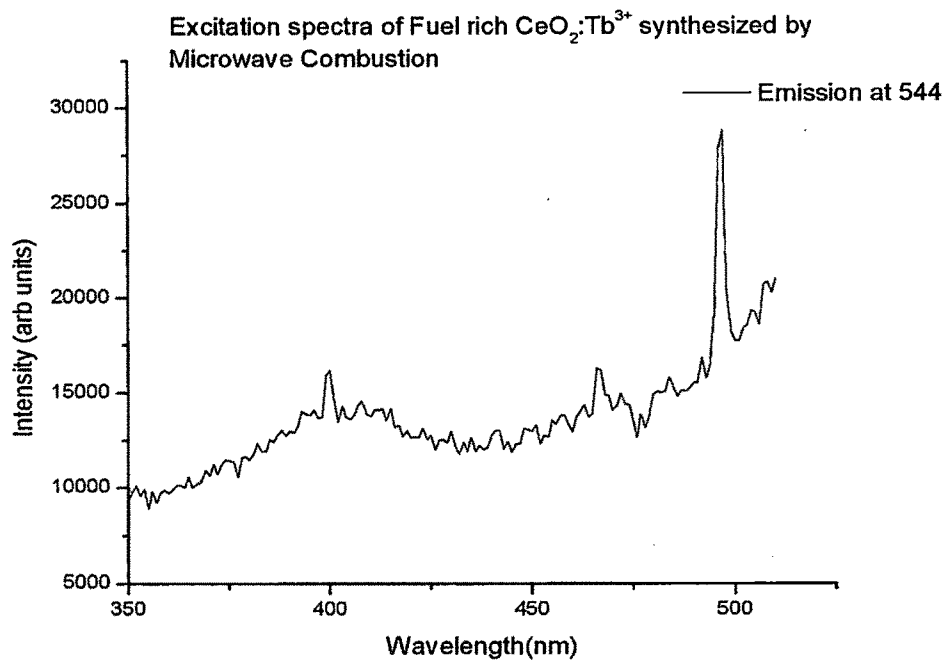
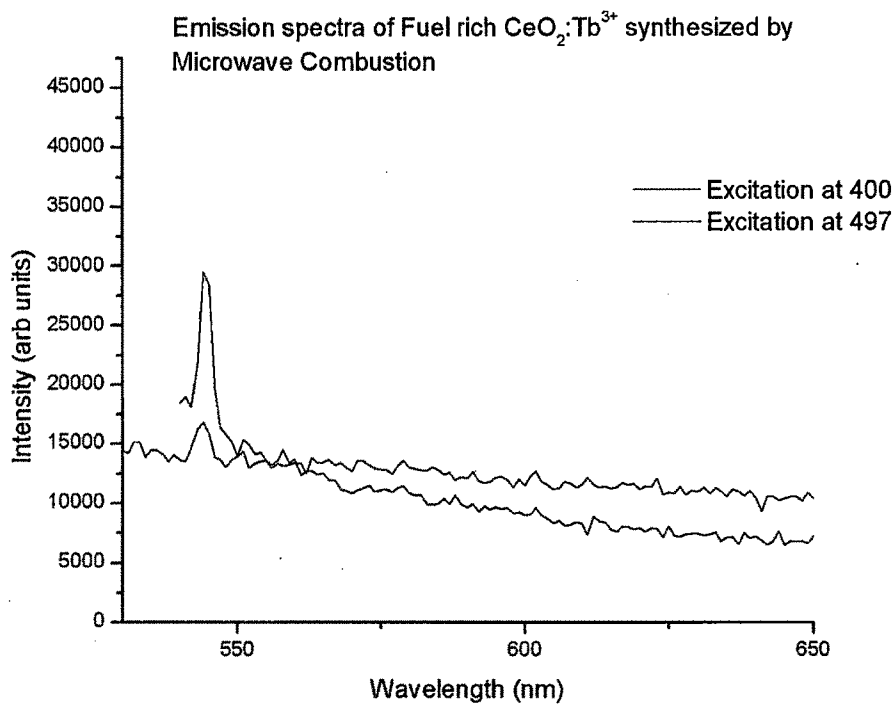


Figure: CTF3b

**Figure: CTF4a****Figure: CTF4b**

**Figure: CTF5a****Figure: CTF5b**

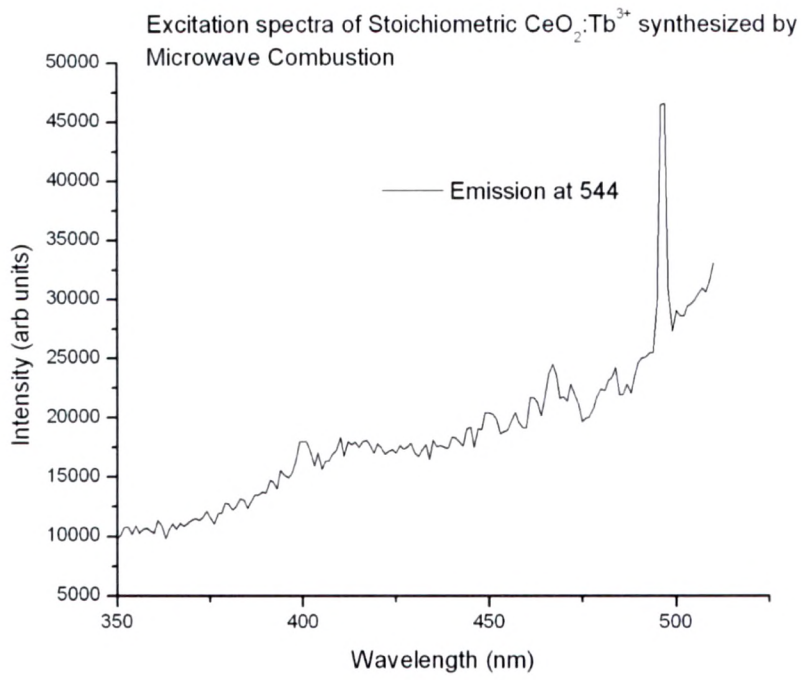


Figure: CTF6a

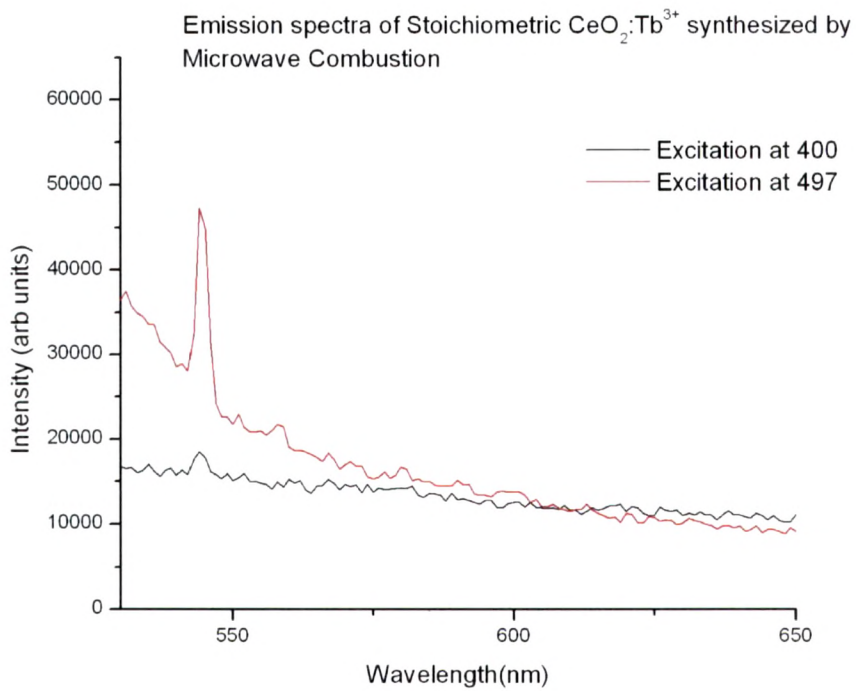
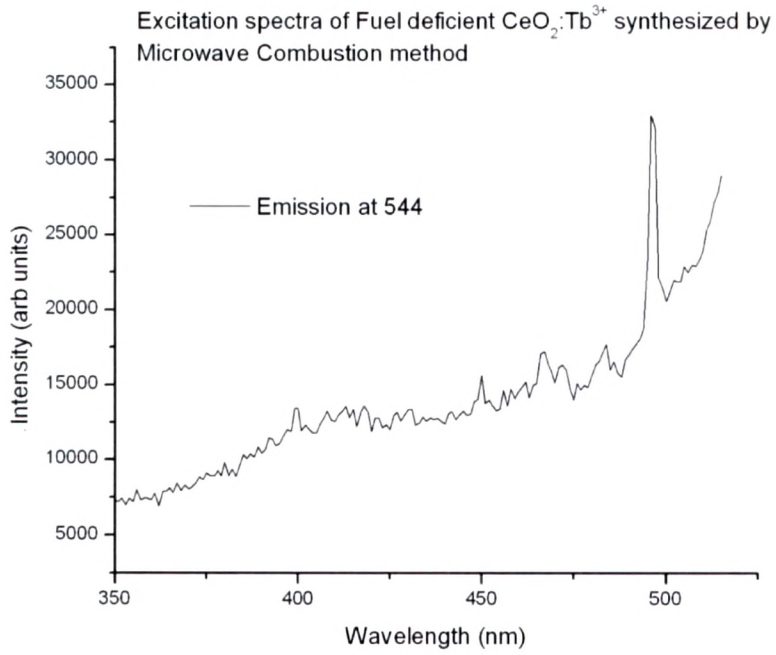
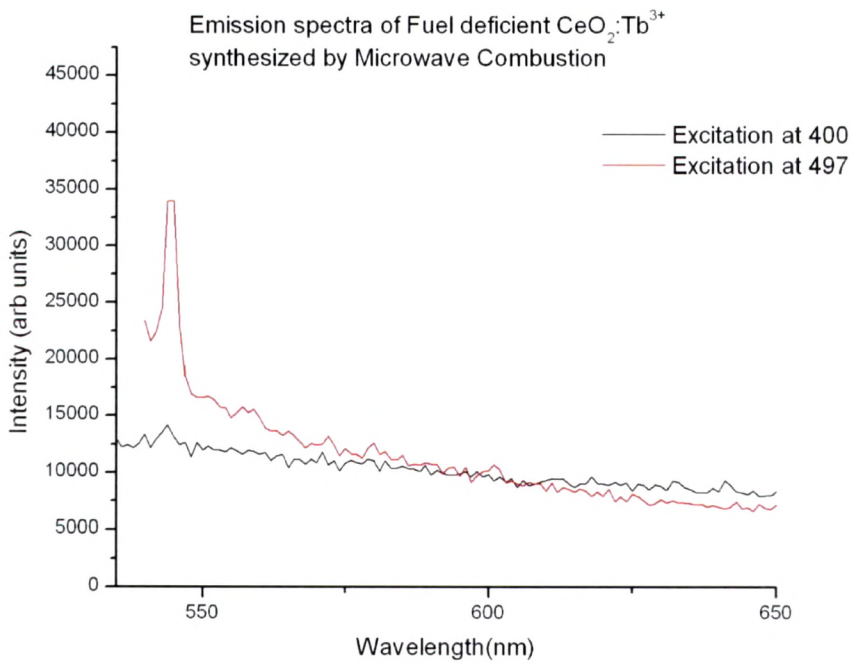
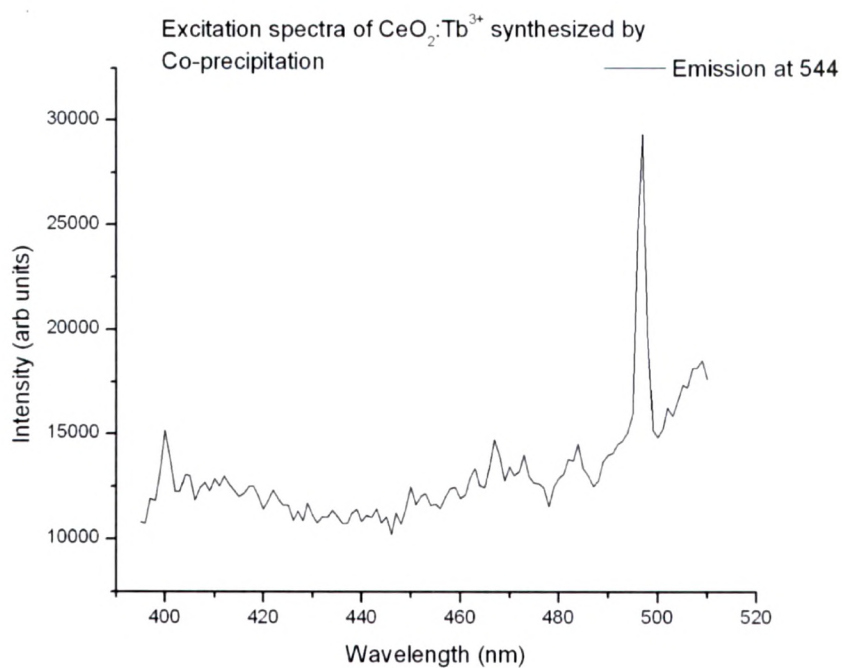
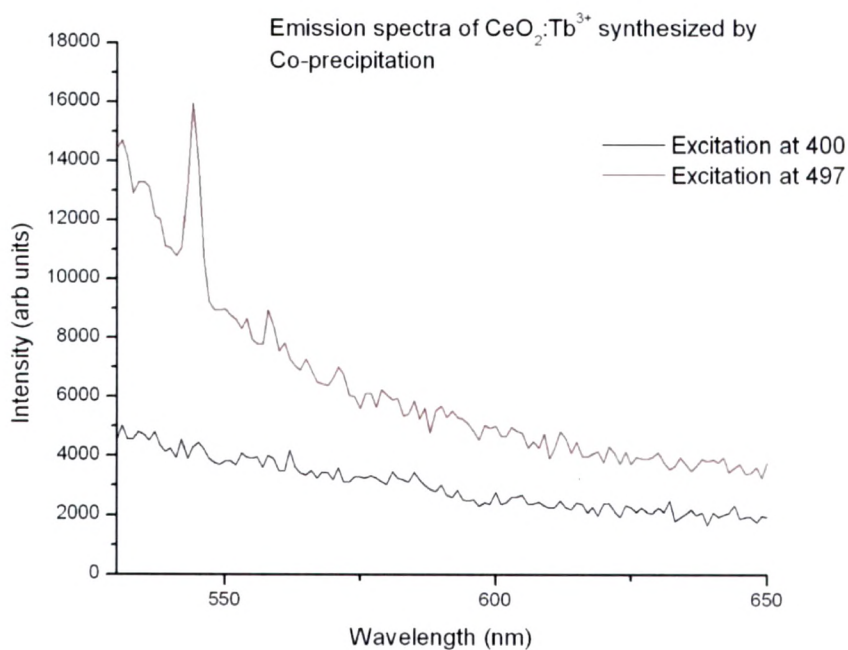
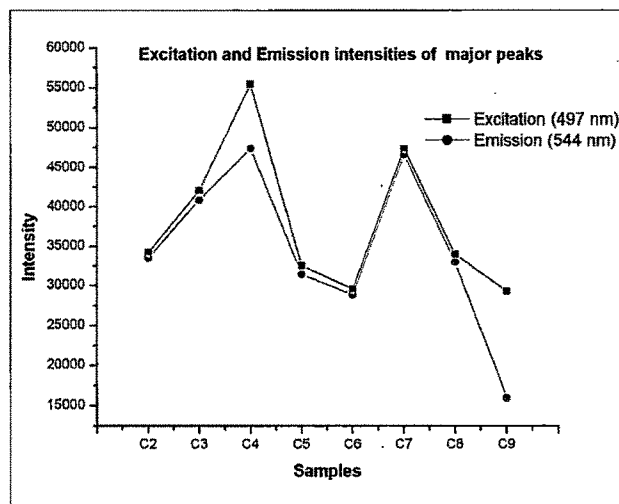


Figure: CTF6b

**Figure: CTF7a****Figure: CTF7b**

**Figure: CTF8a****Figure: CTF8b**

Although the emission characteristics are quite subdued, the singular emission feature at 544 nm is very distinct. The intensities of the excitation (497 nm) and emission (544 nm) peaks are shown in the figure below.

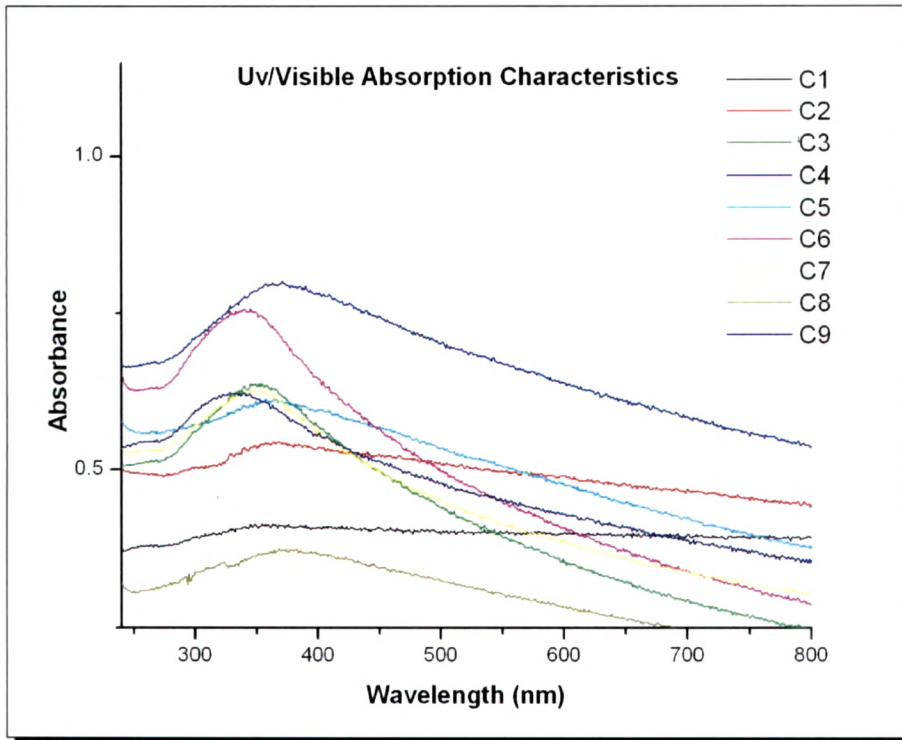


The highest excitation and emission intensities are observed for the samples made by combustion synthesis with stoichiometric proportions of fuel. The lowest emission intensity is for the sample made by co precipitation method. The overall results indicate the poor incorporation of Tb^{3+} ions in the host lattice as effective luminescence centers, either due to charge imbalance or distortion on account of imbalance in the symmetry.

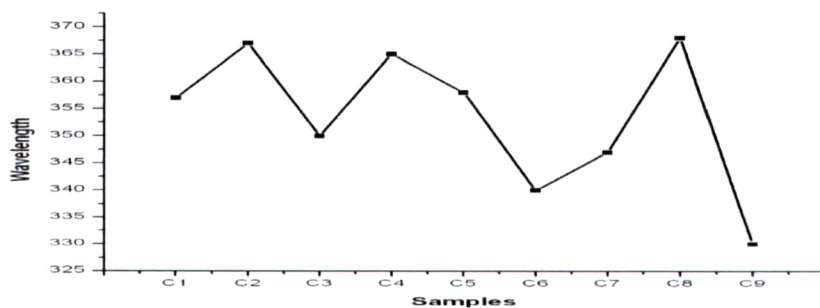
4.3.4 UV – Visible Characteristics

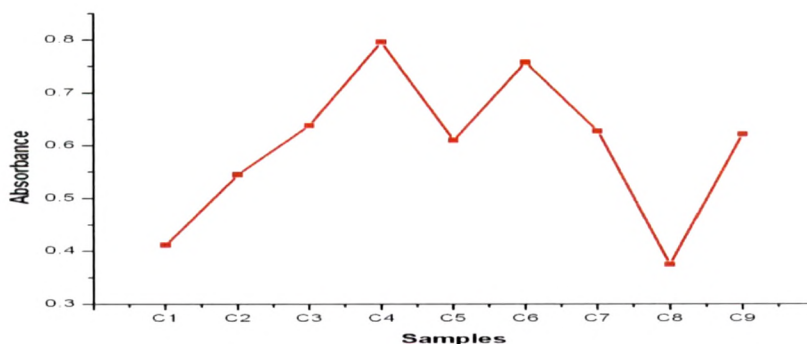
The UV - Visible absorption characteristics of the samples were recorded on a Thermo Fisher Scientific make Evolution 300/600 Spectrophotometer. The light source is a combination of Tungsten halogen and Deuterium lamps.

The samples taken in equal proportion were dispersed in methanol. Each dispersion was sonicated for 30 minutes and then transferred to a quartz cuvette for taking the measurements. The wavelength range was fixed between 240 nm and 800 nm. The results are presented in the figure given below.



There is noticeable variation in the peak absorption wavelength of the different samples. The maximum has been found to be 368 nm while the minimum is at 330 nm. The absorbance also shows a lot of variation from 0.375 to 0.796. The samples used are those activated by Europium. The variation of peak absorption wavelength and absorbance for the different samples is graphically presented below.





The peak absorption wavelength is maximum (368 nm) for the sample C8 (microwave combustion-fuel lean) but it shows the minimum value of absorbance. This looks erratic. This maximum value of peak wavelength is comparable in case of sample C2 (solid state method – 367 nm) and a relatively low absorbance of 0.545. This is a bulk sample with maximum particle size among all samples. The most striking but expected feature is the substantial blue shift of the peak absorption wavelength that occurs in the case of sample C9, which stands quite low at 330 nm. This is a nano particle sample with minimum particle size among all samples. The wavelength and absorbance variations do not exhibit any definitive trend for the samples made by combustion synthesis.

The values of peak absorption wavelength (330 nm – 368 nm) in the UV-Vis spectra are in good agreement with the peak excitation wavelengths (345 nm – 367 nm) of the broad band excitation peaks in the fluorescence spectra.

References

1. Molycorp Inc., Cerium: A Guide to its Role in Chemical Technology, USA, 1995
2. S. Tsunekawa, T. Fukuda, A. Kasuya, *J. Applied Physics* 87 (3) (2000) 1318
3. M. Yamashita, K. Kameyama, S. Yabe, S. Yoshida, T. Kawai, T. Sato, *J. Materials Science* 37 (4) (2002) 683
4. H. Abdul, Y. Iskandar, *Catalysis Today* 96 (3) (2004) 165
5. M. Fathi, E. Bjorgum, O.A. Rokstad, *Catalysis Letters* 72 (1–2) (2001) 25
6. H. Inaba, H. Tagawa, *Solid State Ionics* 83 (1–2) (1996) 1
7. Etsell, T. H.; Flengas, S. N. *Chemical Review* 1970, 70, 339
8. Subbarao, E. C.; Maiti, H. S. *Solid State Ionics* 1984, 11, 317
9. F.H. Garzon, R. Mukundan, E.L. Brosha, *Solid State Ionics* 136/137 (2000) 633
10. Wang, Z. L.; Feng, X. D. *J. Physical Chemistry B* 2003, 107, 13563
11. Miki, T.; Ogawa, T.; Haneda, M.; Kakuta, N.; Ueno, A.; Tateishi, S.; Matsuura, S.; Sato, M. *J. Physical Chemistry* 1990, 94, 6464
12. Amit Kumar, Suresh Babu, Ajay Singh Karakoti, Alfons Schulte, and Sudipta Seal. *Langmuir* 2009 25(18),10998 – 11007
13. Li, L.; Tao, J.; Pan, H.; Chen, H.; Wu, X.; Zhu, F.; Xu, X.; Tang, R. *J. Materials Chemistry* 2008, 18, 5363
14. N. V. Skorodumova, R. Ahuja, S. I. Simak, I. A. Abrikosov, B. Johansson, and B. I. Lundqvist *Physical Review B*, Vol 64, 115108
15. Ralph W. G. Wyckoff, *Crystal Structures, Second Edition, Volume 1*, Interscience publishers
16. Wu, J.; Wang, G. L.; Jin, D. Y.; Yuan, J. L.; Guan, Y. F.; Piper, J. *Chemical Communication* 2008, 3, 365.
17. A.M. Garrido Pedrosa, J.E.C. da Silva, P.M. Pimentel, D.M.A. Melo, F.R.G. e Silva. *J. of Alloys and Compounds* 374 (2004) 223–225
18. T. Ami, Y. Yoshida, N. Nagasawa, A. Machida, M. Suzuki, *Applied Physics Letters* 78 (2001) 1361.
19. D.Q. Shi, M. Inoescu, T.M. Silver, S.X. Dou, *Physica C* 384 (2003)475
20. R.P. Netterfleld, W.G. Sainty, P.J. Martin, S.H. Sie, *Applied Optics* 24 (1985) 2267
21. W.C. Choi, H.N. Lee, Y. Kim, H.M. Park, E.K. Kim, *Japanese J. Applied Physics* 38 (Part 1) (1999) 6392

22. G. Fei, L.I. Guo-hua, Z. Jian-Hui, Q. Fu-Guang, et al., *Chinese Physical Letters*. 18 (2001) 443
23. Shinobu Fujihara and Masashi Oikawa. *J. Applied Physics*, Vol. 95, No. 12, 15 June 2004
24. K. G. Cho, D. Kumar, P. H. Holloway, and R. K. Singh, *Applied Physics Letters* **73**, 3058 1998.
25. S. Itoh, H. Toki, K. Tamura, and F. Kataoka, *Japanese J. Applied Physics, Part 1* **38**, 6387 1999.
26. M. Yu, J. Lin, Y. H. Zhou, and S. B. Wang, *Materials Letters* **56**, 1007 2002
27. E. Danielson, M. Devenney, D. M. Giaquinta, J. H. Golden, R. C. Haushalter, E. W. McFarland, D. M. Poojary, C. M. Reaves, W. H. Weinberg, and X. D. Wu, *Science* **279**, 837 1998
28. Lee, Y. E.; Norton, D. P.; Budai, J. D.; Rack, P. D.; Potter, M. D. *Applied Physics Letters* **2000**, 77, 678.
29. Goubin, F.; Rocquefelte, X.; Whangbo, M. H.; Montardi, Y.; Brec, R.; Jobic, S. *Chemistry Materials* **2004**, 16, 662
30. Hirai, T.; Kawamura, Y. *J. Physical Chemistry B* **2004**, 108, 12763
31. McBride, J. R.; Hass, K. C.; Poindexter, B. D.; Weber, W. H. *J. Appl. Phys.* **1994**, 76, 2435.
32. Mnt, L.; Trudeau, A. T.; Ying, J. Y. *Surface Interface Analysis* **1995**, 23, 219.
33. Marabelli, F.; Wachter, P. *Physical Review B* **1987**, 36, 1238
34. Sun, C.; Li, H.; Zhang, H.; Wang, Z.; Chen, L. *Nanotechnology* **2005**, 16, 1454
35. Green, W. H.; Le, K. P.; Grey, J.; Au, T. T.; Sailor, M. J. *Science* **1997**, 276, 1826
36. J, A.; Garcia, A.; Remo; Piqueras, J. *Physica. Status Solidi A* **1985**, 89, 237
37. Liu, X.; Chen, S.; Wang, X. *J. Luminescence*. **2007**, 127, 650
38. Guo, H.; Qiao, Y. *Appl. Surface Science* **2008**, 254, 1961
39. Zhenling Wang, Zewei Quan, and Jun Lin. *Inorganic Chemistry*, Vol. 46, No. 13, 2007
40. S.T. Aruna and K.C. Patil, *Nano Structured Materials* Vol. 10. No. 6. 1998, 955-964.
41. R.D. Purohita, B.P. Sharma, K.T. Pillai, A.K. Tyagi, *Materials Research Bulletin* 36 (15) 2001, 2711

42. E. Nachbaur, E. Baumgartner and J. Schober, Proceedings of the 2nd European Symposium on Thermal Analysis (1981), 417.
43. A. M. Wynne, J. Chem. Educ. 64 (1987) 180
44. J. J. KINGSLEY and K.C. PATIL, Materials letters, 6,198, 427-432
45. G. K. Adams, WG. Parker and H.G. Wolfhard, Discussions Faraday Society 14, 1953, 97.
46. A K Tyagi, International Symposium on Advanced Materials and Processing, 6-8 December 2004, I. I. T, Kharagpur, India
47. Lina Gu, Guangyao Meng, Materials Research Bulletin, 2007
48. S. Dutta, Q. Mohammad, S. S. Manoharan, J. Materials Science Letters 21, 2002, 1077 – 1079
49. S. Das, A K Mukhopadhyay, S. Datta and D. Basu, Bulletin Materials Science, 32, No. 1, 2009, 1–13.
50. M. Kitiwan, D. Aton, JSME international Journal Series A Vol. 49 No. 1, 2006
51. Xiangting DONG and Guangyan HONG, J. Mater. Sci. Technol, Vol.21 No.4, 2005
52. B. Djuricic, S. Pickering, J. European Ceramic Society 19 (1999) 1925–1934.
53. Sanjay R. Dhage, S. P. Gaikwad, Violet Samuel and V Ravi, Bulletin Materials Science, Vol. 27, No. 3, 2004, 221–222
54. L. A. Chick, G. D. Maupin, L. R. Pederson, Nanostructured Materials Vol. 4 No 5, 1994, Pg 603-615
55. Xiaohua Liu, Shaojun Chen, Xiaodong Wang. J.Luminescence, 2007
56. M. Gaft, G. Panczer, R. Reisfeld, I. Shinno, B. Champagnon, G. Boulon, J. Lumin. 87–89 (2000) 1032.
57. Judd B. R., Physical Review, 127, 750, 1962
58. Ofelt G. S., J. Chemical Physics 37, 511, 1962
59. Suresh Babu, Alfons Schulte and Sudipta Seal., Applied Physics Letters, 2008, 92, 123112
60. E Pereyra-Perea, M R Estrada-Yañez and M García, J. Physics D: Applied Physics 31 (1998) L7–L10